

Electrostatic tuning of the pre- and post-hydrolytic open states in CFTR

Jingyao Zhang^{1,2} and Tzyh-Chang Hwang^{1,2,3}

¹Department of Biological Engineering, ²Dalton Cardiovascular Research Center, and ³Department of Medical Pharmacology and Physiology, University of Missouri, Columbia, MO 65211

Cystic fibrosis transmembrane conductance regulator (CFTR) is an ion channel that couples adenosine triphosphate (ATP) hydrolysis at its nucleotide-binding domains to gating transitions in its transmembrane domains. We previously reported that the charge-neutralized mutant R352C shows two distinct open states, O₁ and O₂. The two states could be distinguished by their single-channel current amplitudes: O₁ having a smaller amplitude (representing a prehydrolytic open state) and O₂ having a larger amplitude (representing a post-hydrolytic open state). In this study, a similar phenotype is described for two mutations of another pore-lining residue, N306D and N306E, suggesting that alterations of the net charge within CFTR's pore confer this unique conductance aberration. Because moving either of the two endogenous charges, R303 and R352, to positions further along TM5 and TM6, respectively, also results in this O₁O₂ phenotype, we conclude that the position of the charged residue in the internal vestibule affects hydrolysis-dependent conductance changes. Furthermore, our data show that the buffer and CFTR blocker morpholino propane sulfonic acid (MOPS⁻) occludes the O₁ state more than it does the O₂ state when the net charge of the internal vestibule is unchanged or increased. In contrast, when the net charge in the internal vestibule is decreased, the differential sensitivity to MOPS⁻ block is diminished. We propose a three-state blocking mechanism to explain the charge-dependent sensitivity of prehydrolytic and post-hydrolytic open states to MOPS⁻ block. We further posit that the internal vestibule expands during the O₁ to O₂ transition so that mutation-induced electrostatic perturbations within the pore are amplified by the smaller internal vestibule of the O₁ state and thus result in the O₁O₂ phenotype and the charge-dependent sensitivity of the two open states to MOPS⁻ block. Our study not only relates the O₁O₂ phenotype to the charge distribution in CFTR's internal vestibule but also provides a toolbox for mechanistic studies of CFTR gating by ATP hydrolysis.

INTRODUCTION

The function of CFTR as a tightly regulated anion-selective ion channel makes it a unique member of the ATP-binding cassette (ABC) protein superfamily, whose members are mostly active transporters carrying a broad range of substrates across the cell membrane against their electrochemical gradients (Davidson and Maloney, 2007; Oldham et al., 2008; Kathawala et al., 2015). The ion translocation pathway, or the pore, of CFTR is proposed to be formed by its two transmembrane domains (TMDs) 1 and 2 (Hwang and Kirk, 2013), each of which contains six transmembrane segments, namely TM1 to TM6 and TM7 to TM12, respectively (Riordan et al., 1989; Bear et al., 1992). Opening and closing of the gate in the TMDs are mainly controlled by ATP binding/hydrolysis at CFTR's two cytosolic nucleotide-binding domains (NBDs), 1 and 2 (Higgins and Linton, 2004; Vergani et al., 2005; Gadsby et al., 2006; Hwang and Sheppard, 2009; Locher, 2009; Rees et al., 2009). The two sets of TMD–NBD complexes in CFTR are linked by a unique, disordered regulatory domain (Ostedgaard et al., 2000, 2001; Bozoky et al., 2013), phosphorylation of which is a prerequisite for CFTR's activity (Chen and Hwang, 2008; Hwang and Sheppard, 2009).

Our understanding of the coupling mechanism between the conformational changes in CFTR's TMDs and those in NBDs is still incomplete despite decades of biophysical and biochemical studies. It is, however, widely accepted that after phosphorylation of the regulatory domain by PKA, the transition in TMDs from the closed state to the open state is linked to ATP-mediated NBD1/NBD2 dimerization in a head-to-tail configuration (Vergani et al., 2005; Sohma and Hwang, 2015). Two gating models relating the molecular motions of NBDs and TMDs have emerged recently (Csanády et al., 2010; Jih and Hwang, 2012; Jih et al., 2012). The strict coupling gating model dictates that opening of the gate in TMDs is triggered by the dimerization of NBDs, whereas gate closure is associated with hydrolysis-induced partial separation of the NBD dimer (Tsai et al., 2009, 2010; Csanády et al., 2010), resulting in a one-to-one stoichiometry between the gating cycle and ATP hydrolysis cycle. However, the energetic coupling model portrays a probabilistic relationship between NBD dimerization and gate opening: NBD dimerization makes the gate more likely to open and vice versa (Jih and Hwang, 2012).

Correspondence to Tzyh-Chang Hwang; hwangt@health.missouri.edu

Abbreviations used: ABC, ATP-binding cassette; cryo-EM, cryo-electron microscopy; DTT, dithiothreitol; NBD, nucleotide-binding domain; PP_i, pyrophosphate; TMD, transmembrane domain.

© 2017 Zhang and Hwang This article is distributed under the terms of an Attribution–Noncommercial–Share Alike–No Mirror Sites license for the first six months after the publication date (see <http://www.rupress.org/terms/>). After six months it is available under a Creative Commons License (Attribution–Noncommercial–Share Alike 4.0 International license, as described at <https://creativecommons.org/licenses/by-nc-sa/4.0/>).



To understand the coupling mechanism of CFTR gating, it would be very helpful if the pre- and post-hydrolytic states could be captured in a single-channel recording. Gunderson and Kopito (1995) were the first to do just that; they identified two open-channel levels in each opening burst (O_1 with a smaller and O_2 with a larger single-channel conductance) and found a preferred opening/closing pattern of $C \rightarrow O_1 \rightarrow O_2 \rightarrow C$ transition over $C \rightarrow O_2 \rightarrow O_1 \rightarrow C$, an observation that is consistent with the idea of a free energy input from ATP hydrolysis to drive the $O_1 \rightarrow O_2$ transition (Gunderson and Kopito, 1995). However, these two conductance levels with WT CFTR are not consistently seen by others. Then, Ishihara and Welsh (1997) found that this observed conductance difference is the result of differential sensitivity of these two open-channel conformations to pore blockade by the negatively charged buffer $MOPS^-$, suggesting that there is little intrinsic difference in chloride permeation between these two open states.

Recently, we accidentally found that the mutant R352C or Q, in the absence of $MOPS^-$, exhibits two distinct open-channel conductance levels (O_1 and O_2) with a similar preferred gating pattern of $C \rightarrow O_1 \rightarrow O_2 \rightarrow C$ transition over $C \rightarrow O_2 \rightarrow O_1 \rightarrow C$ (Jih et al., 2012), where O_1 and O_2 represent pre- and post-hydrolytic open states, respectively. This study raises two interesting questions. First, is this phenotype unique to mutations at position 352, a pore-lining residue in TM6? Second, what is the structural mechanism for the different conductance levels observed for the pre- and post-hydrolytic open-channel conformations?

Following up on our previous substituted cysteine accessibility methodology study of CFTR's TM5 (Zhang and Hwang, 2015), we observed two open-channel conductance levels when the N306C mutant in a Cysless background was modified by $MTSES^-$ (2-sulfonatoethyl MTS) but not by $MTSET^+$ (2-trimethylaminoethyl MTS). Statistical analysis of opening/closing transitions revealed a preferred pattern of $C \rightarrow O_1 \rightarrow O_2 \rightarrow C$ transition over $C \rightarrow O_2 \rightarrow O_1 \rightarrow C$, similar to those seen in R352C. Furthermore, the O_1O_2 phenotype observed with N306D and N306E mutations under the WT background confirmed the idea that a net subtraction of a positive charge (R352C or Q and N306D or E) in the internal vestibule of the pore is responsible for the O_1O_2 phenotype. Interestingly, even with the net charge unaltered, moving the endogenous, positively charged side chain (R303 or R352) along TM5 or TM6 also confers this unique phenotype. We next used $MOPS^-$ to investigate the possible structural basis for the difference in conductance between O_1 and O_2 . Our data show that in most cases, the O_1 state is more sensitive to the channel-impermeant blocker $MOPS^-$ than the O_2 state. More interestingly, this differential sensitivity to $MOPS^-$ is itself susceptible to the net charge in the internal vestibule. An expansion movement of the transmembrane

segments coupled to ATP hydrolysis and a two-step scheme for $MOPS^-$ block are proposed to explain these observations.

MATERIALS AND METHODS

Mutagenesis and channel expression

CFTR mutants in this study were constructed based on two CFTR backgrounds: WT background or Cysless background where all 18 endogenous cysteines were replaced with serine or leucine as reported previously (Bai et al., 2010). Site-directed mutagenesis was performed using the QuikChange XL kit (Agilent Technologies). All mutations were subsequently confirmed by DNA sequencing (DNA core; University of Missouri-Columbia). Together with peGFP-C3 (Takara Bio Inc.) encoding the GFP, the cDNA constructs of CFTR were cotransfected using PolyFect transfection reagent (QIAGEN) into Chinese hamster ovary cells, which were incubated at 37°C in Dulbecco's modified Eagle's medium containing 10% fetal bovine serum. The transfected cells were transferred onto 35-mm tissue culture dishes containing one layer of sterilized glass chips for cells to grow on and incubated at 27°C for 2–7 d before electrophysiological experiments were performed.

Electrophysiology

All experiments were performed in the excised inside-out configuration. Micropipettes made of borosilicate capillary glass were pulled with a two-stage vertical puller (Narishige) and then fire polished with a homemade microforge to reach a pipet resistance of 2–5 M Ω when the pipettes were filled with a standard pipet solution (140 mM NMDG-Cl, 2 mM $MgCl_2$, 5 mM $CaCl_2$, and 10 mM HEPES, adjusted to pH 7.4 with NMDG). Glass chips on which transfected cells were grown were placed into a chamber on the stage of an inverted microscope (Olympus) and continuously perfused with a bath solution (145 mM NaCl, 5 mM KCl, 2 mM $MgCl_2$, 1 mM $CaCl_2$, 5 mM glucose, 5 mM HEPES, and 20 mM sucrose, adjusted to pH 7.4 with NaOH). Immediately after a membrane patch reached a seal resistance of >40 G Ω , it was excised and continuously perfused with a standard perfusate ($[Cl^-] = 154$ mM) containing 150 mM NMDG-Cl, 10 mM EGTA, 10 mM HEPES, 8 mM Tris, and 2 mM $MgCl_2$, adjusted to pH 7.4 with NMDG. For $[Cl^-]$ -dependent experiments in Fig. 6, high $[Cl^-]$ pipette solution containing ($[Cl^-] = 374$ mM) 360 mM NMDG-Cl, 2 mM $MgCl_2$, 5 mM $CaCl_2$, and 10 mM HEPES, adjusted to pH 7.4 with NMDG, was used to avoid a drastic osmolarity difference across the membrane. Perfusion solutions with different concentrations of chloride ions were made with 375 mM NMDG-Cl, 10 mM EGTA, 10 mM HEPES, 8 mM Tris, and 2 mM $MgCl_2$, adjusted to pH 7.4 with NMDG for $[Cl^-] = 379$ mM; 750 mM NMDG-Cl, 10 mM EGTA,

10 mM HEPES, 8 mM Tris, and 2 mM MgCl₂, adjusted to pH 7.4 with NMDG for [Cl⁻] = 754 mM; and 1,125 mM NMDG-Cl, 10 mM EGTA, 10 mM HEPES, 8 mM Tris, and 2 mM MgCl₂, adjusted to pH 7.4 with NMDG for [Cl⁻] = 1,129 mM. The 2 mM ATP solution containing 30 mM MOPS⁻ in Fig. 8 was adjusted to pH 7.5 with NMDG to ensure at least two thirds of the MOPS (FisherBiotech) molecules were in its negatively charged form as MOPS⁻, which was proposed to be the effective form for blocking CFTR (Ishihara and Welsh, 1997). Experiments were conducted at room temperature (22–24°C). Current signals at different holding potentials (-50, -80, or 50 mV) as required for different experimental purposes were acquired with a patch-clamp amplifier (EPC9; HEKA), filtered at 100 Hz, digitized online at 500 Hz with Pulse software (version 8.53; HEKA), and captured onto a hard disk. Fast solution exchange was achieved with a commercial solution exchange system (SF-77B Perfusion Fast-Step; Warner Instruments).

Reagents and cysteine modification

MTS reagents (MTSES⁻ and MTSET⁺; Toronto Research Chemicals Inc.) were prepared as 100 mM stock solutions in distilled deionized H₂O and stored at -70°C. A single aliquot of the stock solution was thawed immediately before use and diluted into the perfusion solution with 2 mM ATP (Sigma-Aldrich) to modify the mutants in the presence of ATP (Figs. 1, S2, and S6). Pyrophosphate (PP_i) was purchased from Sigma-Aldrich. To prevent the thiol group of engineered cysteine from undergoing spontaneous oxidation (Li et al., 2005; Liu et al., 2006), we routinely added 2.67 mM dithiothreitol (DTT; Sigma-Aldrich) to the perfusion solution containing 32 IU/ml PKA and 2 mM ATP in inside-out experiments.

Data analysis

The single-channel amplitudes of the O₁ state and O₂ state for most of the mutants exhibiting a clear O₁O₂ phenotype were measured by fitting the distributions in all-points histograms with a built-in multi-Gaussian function (Igor 6.3). For some mutants with a smaller difference in the single-channel amplitudes between the O₁ and O₂ states such as R352Q and S307R/R303C/Cysless, the all-points histogram method is not sensitive enough to resolve two peaks. In this case, the single-channel current amplitude of each state was measured by treating each opening burst as a "macroscopic" trace. For each macroscopic recording, the single-channel amplitudes of the O₁ and O₂ states were calculated by subtracting the baseline current from the mean macroscopic current amplitudes. At least five opening events of >8 ms in duration in one patch recording were analyzed and averaged for one data point. These averaged single-channel amplitudes of O₁ and O₂ states

from each trace also yielded one set of the absolute and normalized differences between O₁ and O₂ states in Fig. 6 C and one set of F_b for MOPS⁻ block of the two open states in Fig. 9. The final mean and SEM were calculated from more than three recordings.

Statistical analyses in Tables 1 and 2 were done using the same method used in our previous study (Jih et al., 2012). Here we chose 8 ms as the cutoff to identify a state, which represents five data points at the 500-Hz sampling rate, to avoid counting non-CFTR static spikes or noises (three data points, or 4 ms, to define an event of current rise/drop). This criterion should minimally affect our topological analysis of gating patterns because the mean burst durations of the O₁ state and the O₂ state are 116 ms and 55 ms, respectively, for N306D and 135 ms and 100 ms for M348R/R352Q measured by dwell-time histograms (Fig. S1). Current traces recorded at negative voltage were presented in all figures as upward deflections except in Figs. 7 and 8 E, where positive currents were presented as upward deflections. The transmembrane segments (TM6, TM5, and TM12) in the cartoon in Fig. 10, Fig. S3, and Fig. S4 were extracted from the open-channel homology model built by Dalton et al. (2012) and rearranged for cosmetic purposes to show the proposed change in volume of the internal vestibule upon the O₁ to O₂ transition. To more accurately illustrate the relative positions among the residues of interest in Fig. 4, we adopted the first high-resolution cryo-electron microscopy (cryo-EM) structure of CFTR, which was published in Zhang and Chen (2016). Although this atomic structure represents zebrafish CFTR, because the current as well as previous functional experiments were performed in human orthologues, residues in this cryo-EM structure were discussed in accordance with their corresponding positions in human CFTR. All the pictures extracted from the homology model or cryo-EM structure of CFTR were prepared with PyMOL (version 1.3; Schrödinger). All results are presented as means ± SEM; *n* is the number of experiments.

Online supplemental material

Fig. S1 shows dwell-time histograms for the O₁ state, O₂ state, and opening burst in N306D and M348R/R352Q. Fig. S2 presents data showing that S307C/Cysless, F310C/Cysless, and F311C/Cysless modified by MTS ET⁺ show only one conductance level. Fig. S3 shows a two-state model for differential MOPS⁻ block between the O₁ and O₂ states. Fig. S4 shows a three-state model for MOPS⁻ differential blocking. Fig. S5 shows that neutralization of D993 affects the O₁O₂ phenotype in N306D. Fig. S6 shows that modification of S307R/R303C/Cysless and A299R/R303C/Cysless with thiol-specific reagents changes their O₁O₂ phenotype. Table S1 shows a sample set of simulation parameters using the two-step scheme for MOPS⁻ block.

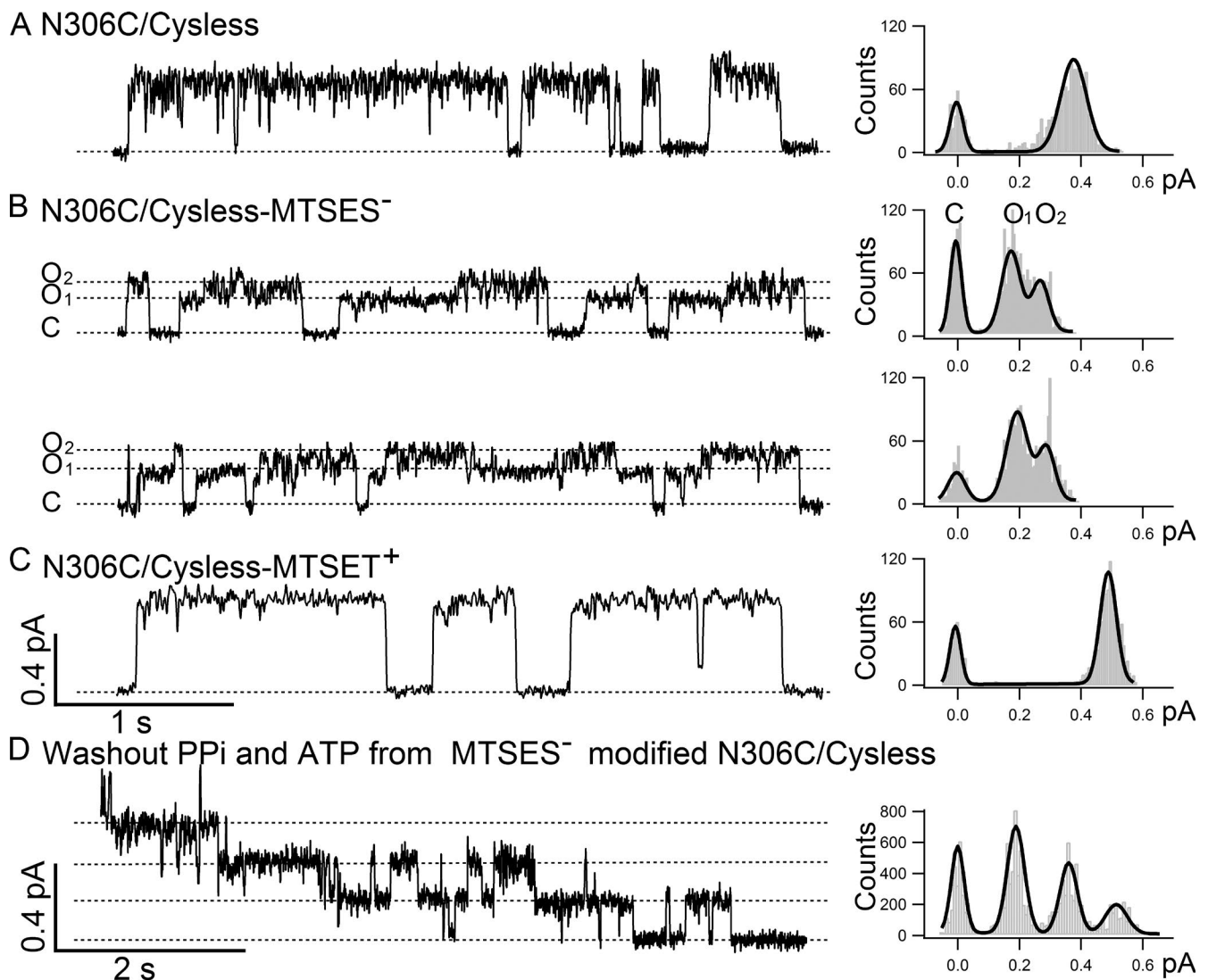


Figure 1. N306C/Cysless modified by MTSES⁻ shows O₁ to O₂ transitions. Single-channel recordings were conducted under -50 mV. (A) The left panel shows a representative single-channel trace of N306C/Cysless, and the all-points histogram on the right side shows only one conductance level (0.40 ± 0.02 pA, $n = 14$). (B) Single-channel recordings of N306C/Cysless modified by negatively charged thiol-specific reagent MTSES⁻ show two distinct single-channel conductance levels: a small one, O₁ (0.19 ± 0.02 , $n = 3$), and a large one, O₂ (0.30 ± 0.02 , $n = 3$), with a preferred transition order of C→O₁→O₂→C. The difference between two open-channel conductance levels is clearly differentiated in the all-points histogram on the right. (C) In contrast, N306C/Cysless modified by positively charged thiol-specific reagent MTSET⁺ shows a single and yet larger open-channel current amplitude (0.49 ± 0.02 , $n = 4$) compared with the one before modification in A. (D) A representative recording of the washout phase of a macroscopic current trace using ATP-free perfusion solution from a patch containing multiple MTSES⁻-modified N306C/Cysless channels locked open by PP_i and ATP. The stepwise closing of each channel is shown in the trace on the left, and the long burst duration in the absence of ATP before channels close is indicative of these channels being locked open by PP_i and ATP into an open-channel conformation with two NBDs in a head-to-tail dimeric configuration. The single-channel amplitude (0.19 ± 0.01 , $n = 4$) measured in the all-points histogram on the right is identical to the single-channel amplitude of the O₁ state in B.






RESULTS

Adding one negative charge at position 306 of CFTR's TM5 results in two distinct open-channel conductance levels: O₁ and O₂

In our previous cysteine-scanning study on the fifth transmembrane segment (TM5) of CFTR, we identified six pore-lining residues along this transmembrane segment

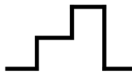




(Zhang and Hwang, 2015). All six pore-lining residues, A299, R303, N306, S307, F310, and F311, are proposed to form part of the internal vestibule of CFTR's pore, as they are only accessible to thiol-specific reagent such as MTSES⁻ and MTSET⁺ from the intracellular side of the membrane. Although the modification of the cysteine residue introduced at each of the positions mentioned in the previous section with negatively charged MTSES⁻ re-

Table 1. Summary of opening events by different gating patterns in N306C/Cysless modified by MTSES⁻

	O ₁ -O ₂	O ₁	O ₂	O ₂ -O ₁	(O ₁ -O ₂) ⁿ	Total
Gating topology						
No. of events	730	480	119	15	148	1,492
Percentage	49%	32%	8%	1%	10%	100%

Five categories of gating topologies are illustrated at the top of the table. The number of events and percentage for each topology are displayed. Bursts were categorized as described in Materials and methods. Data in this table show that C→O₁→O₂→C is the preferred gating pattern, and a considerable amount of events with more than one O₁→O₂ transition were observed in the MTSES⁻-modified N306C/Cysless. Of note, because of the intrinsic instability of the O₂ state, the analysis method used inevitably overestimates the number of events in the second category and underestimates those in the rest of the categories.

Table 2. Summary of opening events by different gating patterns in N306D

	O ₁ -O ₂	O ₁	O ₂	O ₂ -O ₁	(O ₁ -O ₂) ⁿ	Total
N306D-CFTR						
No. of events	491	207	104	13	217	1,032
Percentage	48%	20%	10%	1%	21%	100%

Data in this table show that C→O₁→O₂→C (first category) is the preferred gating topology in N306D.

duced the single-channel amplitude (Zhang and Hwang, 2015), a closer inspection of the MTSES⁻-modified single-channel data revealed an unexpected finding: two distinct open-channel levels were seen in MTSES⁻-modified N306C/Cysless. As shown in Fig. 1 A, the single-channel trace of N306C/Cysless before MTSES⁻ modification exhibits a uniform current amplitude (0.40 ± 0.02 pA, $n = 14$). However, once modified by MTSES⁻, opening bursts with two distinct conductance levels were observed (Fig. 1 B): a smaller O₁ (0.19 ± 0.02 pA, $n = 3$) and a larger O₂ (0.30 ± 0.02 pA, $n = 3$), a phenotype akin to that of the mutant R352C or R352Q that we have characterized previously (Jih et al., 2012). In contrast, for the same mutant N306C/Cysless, the modification by positively charged MTSET⁺ does not yield multiple conductance levels (Fig. 1 C), but it does increase slightly the single-channel amplitude to 0.49 ± 0.02 pA ($n = 4$).

Statistical analysis on the gating behavior of the MTSES⁻-modified N306C/Cysless channels in Table 1 revealed a preferred pattern of C→O₁→O₂→C transition over C→O₂→O₁→C, similar to those seen in R352C (Jih et al., 2012), suggesting a violation of microscopic reversibility that requires a free energy input to drive CFTR gating in a circular manner. To further test whether the O₁ and O₂ states in MTSES⁻-modified N306C/Cysless channels also label prehydrolytic and post-hydrolytic states, we applied 4 mM PP_i, a poorly hydrolyzable phosphate analogue, with 2 mM ATP together to lock open MTSES⁻-modified channels and subsequently washed out all the ligands. As seen in Fig. 1 D, the locked-open channels close one at a time,

resulting in a staircase pattern of current drop. All-points histogram analysis of this part of the recording (Fig. 1 D, right) revealed the single-channel amplitude of each locked-open channel as 0.19 ± 0.01 pA ($n = 4$), which is virtually identical to the single-channel amplitude of the O₁ state shown in Fig. 1 B. The observation that PP_i can lock the MTSES⁻-modified N306C/Cysless channels into the O₁ state supports the idea that the O₁ and O₂ states in MTSES⁻-modified N306C/Cysless channels indeed represent the pre- and post-hydrolytic open states, respectively, because PP_i, like the nonhydrolyzable ATP analogue adenylyl-imidodiphosphate (AMP-PNP), was proposed to lock the channel into an open conformation with a dimerized NBD where its nucleotide-binding site 2 and site 1 were occupied by PP_i and ATP, respectively (Tsai et al., 2009).

To test the hypothesis that the observed difference in single-channel amplitudes between O₁ and O₂ states caused by MTSES⁻ modification is the result of the introduced negative charge rather than any unusual properties of this reagent or Cysless CFTR, we engineered a negative charge directly into WT CFTR at position 306 by making N306D and N306E mutations. Fig. 2 shows representative single-channel traces of N306D and N306E, both of which exhibit similar two open-channel states that are indistinguishable from those of the MTSES⁻-modified N306C/Cysless channels: O₁ = 0.18 ± 0.01 pA and O₂ = 0.24 ± 0.01 pA, $n = 3$, for N306D; O₁ = 0.19 ± 0.01 pA and O₂ = 0.27 ± 0.01 pA, $n = 3$, for N306E. Note in Fig. 2 B, which shows the expanded openings marked in Fig. 2 A, we could also dis-

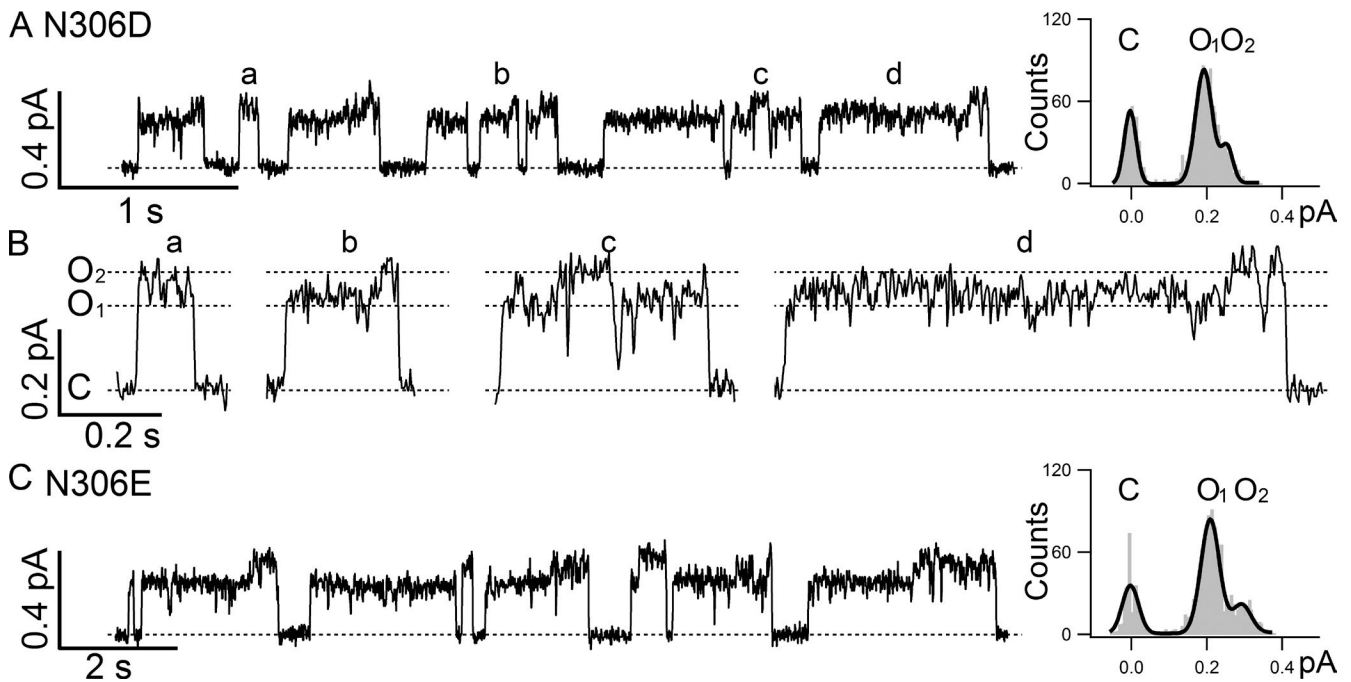


Figure 2. **N306D/E channels present a clear O_1O_2 phenotype.** (A) A representative single-channel recording of N306D in the WT background shows the characteristic O_1O_2 phenotype, supporting the idea that it is the negative charge introduced at position 306 that accounts for the O_1O_2 phenotype displayed in N306D and in MTSES⁻-modified N306C/Cysless. Single-channel amplitudes of O_1 (0.18 ± 0.01 , $n = 3$) and O_2 (0.24 ± 0.01 , $n = 3$) states can be measured in the all-points histogram on the right. (B) Expanded opening bursts show details of each opening events as marked in A. (C) A representative single-channel recording of N306E in the WT background further confirms the role of a negative charge at position 306 in conferring the O_1O_2 phenotype. The all-points histogram shows distinct single-channel amplitudes of the O_1 (0.19 ± 0.01 , $n = 3$) and O_2 states (0.27 ± 0.01 , $n = 3$).

cern a preferred gating pattern of $C \rightarrow O_1 \rightarrow O_2 \rightarrow C$, which is confirmed by statistical analyses of these traces (Table 2). These results support the notion that it is the negative charge introduced to position 306 in the internal vestibule of CFTR's pore that causes the appearance of two subconductance levels, O_1 and O_2 , in an opening burst with preferred O_1 to O_2 transitions, namely, the O_1O_2 phenotype.

The position of charge also determines the O_1O_2 phenotype

As reported previously (Jih et al., 2012), this O_1O_2 phenotype is a distinct characteristic of R352C or Q. We noted here that R352 in TM6 is at a similar topological location as N306 in TM5 (Riordan et al., 1989). Recent computer modeling of CFTR's pore also placed these two residues at the same level in the internal vestibule of CFTR (Dalton et al., 2012; Mornon et al., 2015), a picture confirmed recently by the first high-resolution cryo-EM structure of the whole CFTR protein (see Fig. 4; Zhang and Chen, 2016). It is also interesting to note that the neutralization of the positively charged arginine at position 352 and the introduction of a negative charge side chain at position 306 cause a similar electrostatic effect in the internal vestibule of the pore—a net decrease of a positive charge. The experi-

ments in Fig. 3 demonstrate that this decrease of the positive potential in the internal vestibule, as happened in R352C or Q and N306D or E, is not the only factor that determines the O_1O_2 phenotype. Fig. 3 A shows a representative single-channel trace of R352Q, recorded at the same voltage (-50 mV) as that in Fig. 1 and Fig. 2. As reported previously (Jih et al., 2012), the conductance of R352Q is smaller compared with that of WT channels, and thus the difference between O_1 and O_2 states is barely discernable. (The difference in single-channel amplitude only becomes apparent when $[Cl^-]$ is increased; see Jih et al. [2012] for details.) However, although introducing a positively charged arginine to position 348 in the R352Q background (M348R/R352Q double mutation) increased single-channel current amplitudes for each open state presumably because of partial restoration of the positive potential in the pore, the O_1O_2 phenotype remained (Fig. 3 B). Interestingly, although the absolute difference ($i_{O_2} - i_{O_1}$) in current amplitude between the O_1 and O_2 states becomes larger with the introduction of an arginine at position 348, the relative difference ($(i_{O_2} - i_{O_1})/i_{O_1}$) is unchanged ($55.6 + 5.0\%$ for R352Q, $n = 4$; $50.1 + 4.0\%$ for M348R/R352Q, $n = 4$), suggesting that the arginine at position 348 increases the single-channel amplitude proportionally for both states.

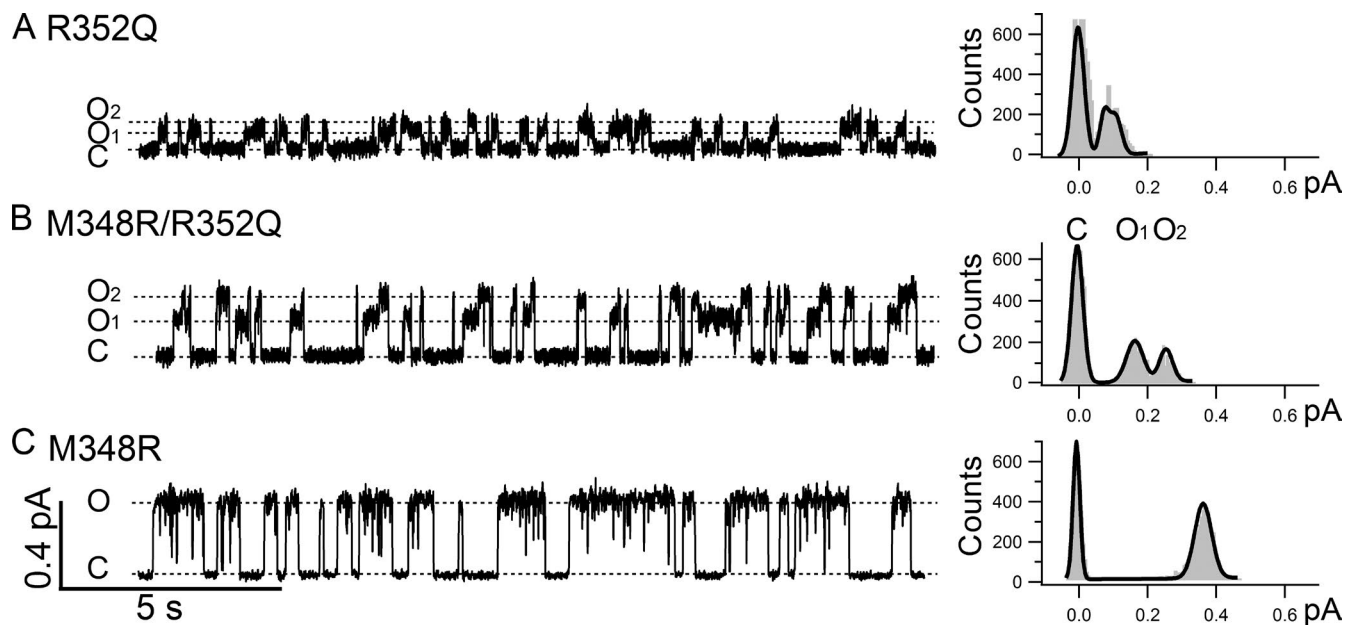


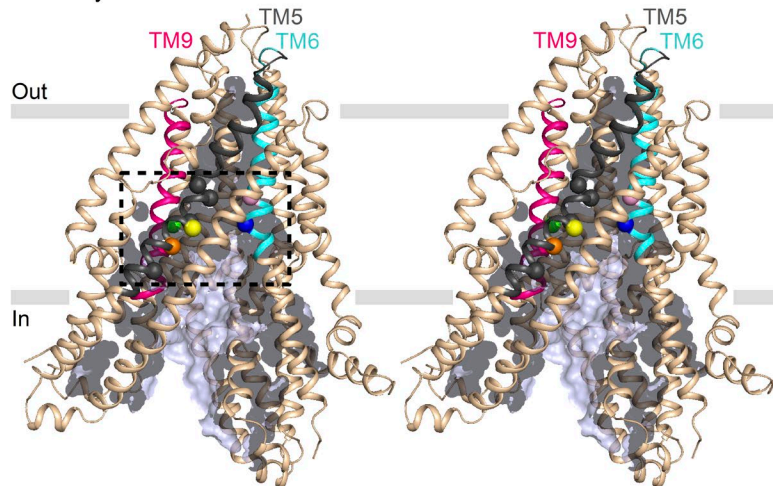
Figure 3. O_1O_2 phenotype revealed by charge displacement in TM6. (A) A representative recording of R352Q barely shows two conductance levels because the single-channel amplitudes of both the O_1 state (0.09 ± 0.01 , $n = 4$) and the O_2 state (0.13 ± 0.01 , $n = 4$) are dramatically reduced because of the neutralization of arginine 352 in the internal vestibule of CFTR. The two peaks in the all-points histogram on the right are mostly coalesced into a single peak. (B) A representative recording of the double mutant M348R/R352Q also displays the O_1O_2 phenotype with much higher single-channel amplitudes for both the O_1 state (0.17 ± 0.01 , $n = 4$) and the O_2 state (0.25 ± 0.01 , $n = 4$) as measured in the all-points histogram on the right. (C) A representative recording of M348R with a single-channel amplitude of 0.35 ± 0.01 ($n = 4$) and the corresponding all-points histogram on the right.

As a control, Fig. 3 C shows a single-channel trace of M348R, which displays only one single open state with an amplitude of 0.35 ± 0.01 pA ($n = 4$) just like WT channels despite one additional positive charge engineered into the pore (Bai et al., 2010; Zhou et al., 2010). Thus, the occurrence of the O_1O_2 phenotype for R352Q is not solely because of a change of the net charge in the internal vestibule; instead, we conclude that the position of the charged residues in TM6 in the internal vestibule of CFTR's pore plays a critical role in determining the O_1O_2 phenotype.

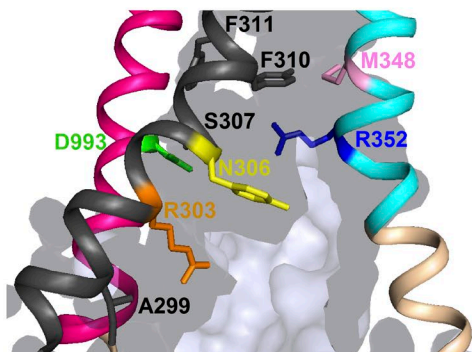
The results shown in Fig. 3 implicate the importance of the location of positive charges in the internal vestibule in deciding the O_1O_2 phenotype. Inspecting the pore-lining residues of TM5, we also found an arginine at position 303, mutations of which have been shown to decrease the single-channel conductance (Aubin and Linsdell, 2006; Zhou and Linsdell, 2007; Zhang and Hwang, 2015). In both the homology model of CFTR's open-channel conformation and the cryo-EM structure of CFTR's prephosphorylated closed conformation (Dalton et al., 2012; Zhang and Chen, 2016), R352, M348, and N306 are spatially close to each other, all residing in the internal vestibule of CFTR's pore (Fig. 4). Furthermore, R303 is just one helical turn internal to N306. The idea that the location of the positively charged residues in TM6 in the internal vestibule plays a critical role in conferring the O_1O_2 phenotype sug-

gests that moving this arginine along TM5 may also result in the O_1O_2 phenotype. Unlike R352C/Cysless, the single mutation R303C/Cysless of neutralizing the arginine at position 303 does not show the O_1O_2 phenotype (see Fig. 8 D). However, just like M348R/R352Q, moving the arginine from position 303 to several other pore-lining positions, including 307, 310, and 311, resulted in the O_1O_2 phenotype (Fig. 5). Interestingly, the larger the distance is between the moved arginine and position 303, the higher the difference is of the single-channel amplitude between O_1 and O_2 . For example, a visual distinction of O_1 and O_2 in the S307R/R303C/Cysless mutant is only possible in high-quality recordings with an exceedingly stable baseline (Fig. 5 A), although a corresponding all-points histogram fails to clearly dissect two conductance levels. However, Fig. 5 (B and C) shows a discernable O_1O_2 phenotype for F311R/R303C/Cysless and F310R/R303C/Cysless. These representative single-channel traces as well as expanded individual opening bursts in Fig. 5 D show telltale signs of irreversible gating (i.e., predominant $C \rightarrow O_1 \rightarrow O_2 \rightarrow C$). The O_1O_2 phenotype displayed here with the double mutants is not caused by the addition of arginine at positions 307, 310, and 311 because simple addition of a positive charge at these positions does not yield the O_1O_2 phenotype (Fig. S2). The existence of the O_1O_2 phenotype requires simultaneous neutralization of the arginine at position 303.

A Cross-Eye Stereo Lateral View of TMDs



B Enlarged View of Squared Region in A



C Top View of TM5, 6 and 9

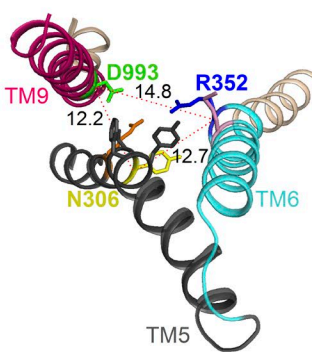


Figure 4. Pore-lining residues along TM5 located spatially close to R352 on TM6. (A) A cross-eye stereo lateral view of CFTR's two TMDs based on the cryo-EM structure of CFTR (Zhang and Chen, 2016). The whole TMD is colored in wheat. TM6 is colored in cyan, TM9 in magenta, and TM5 in black. The pore-lining residues R352 and M348 in TM6 are colored in blue and pink, respectively, the pore-lining residues R303 and N306 along TM5 are colored in orange and yellow, respectively, and A299, S307, F310, and F311 along TM5 are colored in black. D993 in TM9 is colored in green. The surface of the internal vestibule is shown with its aqueous side in light blue and the back side in light blue shadow. From this lateral view, R352 and D993 reside at a critical location where the internal vestibule tapers down to the narrow region. (B) Enlarged view of the boxed region in A. If we use R352/D993 as a reference plane, pore-lining M348, F310, and F311 lie slightly above, whereas N306 lies below, this plane. In contrast, R303 and A299 reside at a more internal and spacious region of the internal vestibule. (C) Top view of TM5, 6, and 9. Distances between the residues were measured in angstroms.

Collectively, the data from the arginine swap experiments in Fig. 5 suggest that, like R352 in TM6, the position of this positively charged side chain of TM5 in the internal vestibule of CFTR's pore is critical in imparting the O_1O_2 phenotype.

Effects of membrane potentials and cytoplasmic $[Cl^-]$ on the O_1O_2 phenotype

It has been proposed that the positively charged residues (arginine/lysine) in the internal and external vestibules of CFTR's pore play important roles in concentrating the charge carrier chloride from the surrounding solutions and hence facilitate high chloride conductance through surface charge effects (Aubin and Linsdell, 2006; Cui et al., 2008; Bai et al., 2010; El Hiani and Linsdell, 2012). As many of our molecular manipulations alter the net charge (e.g., R352Q and N306D), we wonder whether the difference in single-channel amplitudes between the O_1 and O_2 states can be attributed to possible different surface charge effects exerted by the charged side chain. We therefore tested whether increasing $[Cl^-]$ can alter the difference in single-channel amplitudes between the O_1 and O_2 states. The left panel in Fig. 6 A shows representative single-channel opening events of N306D at different concentrations of cytoplasmic chloride ions. The all-

points histograms (Fig. 6 A, right) show that both O_1 and O_2 states are clearly discernable within the experimental chloride range. Fig. 6 B summarizes the single-channel amplitudes of the O_1 and O_2 states for N306D under the indicated conditions. Fig. 6 C shows the absolute difference in single-channel amplitudes between the O_1 and O_2 states (blue open diamonds) and the normalized difference ($\Delta i/i_{O1}$) in single-channel amplitudes between the O_1 and O_2 states (red closed diamonds). Within the range of $[Cl^-]$ tested, neither the absolute difference nor the normalized difference between the O_1 and O_2 states is very sensitive to the changes of $[Cl^-]$. This result, together with the observation that the specific location of the charge plays a major role in deciding the O_1O_2 phenotype, suggest that the surface charge effect is unlikely to account for our observations. Instead, it is more likely that the pre- and post-hydrolytic states assume different pore structures, and the functional consequence—chloride permeation through the pore—of this structural difference is exaggerated by our mutations.

The idea of different pore structures is consistent with the observation that the O_1O_2 phenotype also exists at positive voltage when the chloride ions flow in an opposite direction. Fig. 7 A shows a continuous recording of a single N306D channel at ± 50 mV. In Fig. 7 B, the ex-

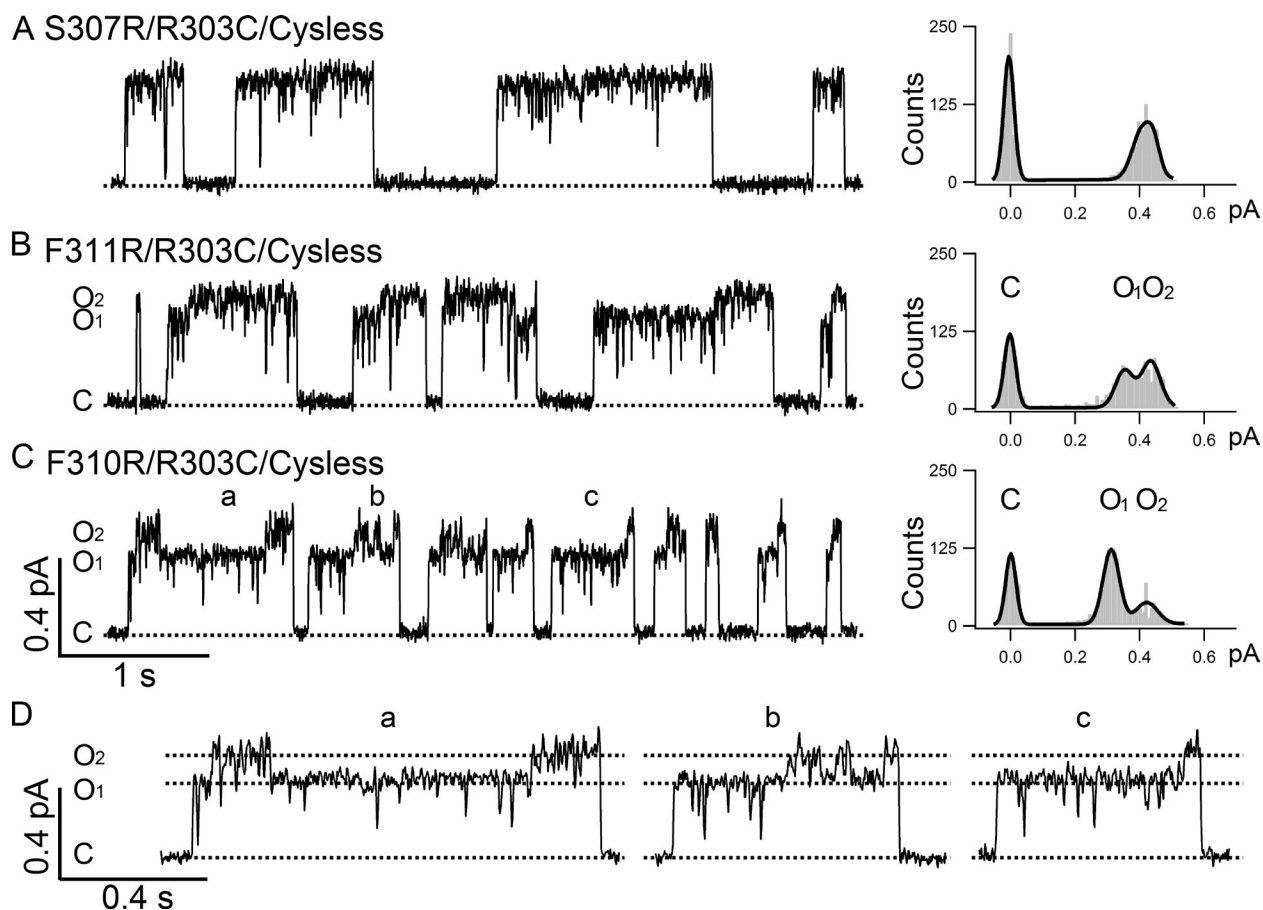


Figure 5. **The position of arginine in TM5 plays a role in determining the current amplitudes of O_1 and O_2 states.** (A) A representative recording of S307R/R303C/Cysless shows a slight and barely discernible difference between the O_1 and O_2 states. But the all-points histogram fails to distinguish these two states. (B) Clear resolution of the O_1 and O_2 states in F311R/R303C/Cysless in both the single-channel trace (left) and all-points histogram (right). (C) A representative recording of F310R/R303C/Cysless on the left shows clearly resolvable two open states reflected as two distinct peaks in the all-points histogram on the right. (D) Expanded opening bursts marked in C to show detailed transitions in a gating cycle. The burst marked c shows a prototypical gating topology of $C \rightarrow O_1 \rightarrow O_2 \rightarrow C$.

panded view of the numbered opening bursts in Fig. 7 A shows two distinct open states and the preferred open transitions of $C \rightarrow O_1 \rightarrow O_2 \rightarrow C$. The existence of the O_1O_2 phenotype at positive voltage is also seen in mutants with the net charge unaltered, e.g., M348R/R352Q (TM6; Fig. 7 C) and F311R/R303C/Cysless (TM5; Fig. 7 D). Thus, we propose that, upon ATP hydrolysis, CFTR's pore undergoes some conformational changes that affect the ion permeation properties; although this functional alteration may not be large enough to become discernable in WT channels, our mutations, by changing charge locations in the internal vestibule, exacerbate the functional consequence of hydrolysis-driven conformational changes in the pore and thus make possible visualization of the O_1 and O_2 states. Because our mutations are all located in the internal vestibule of the pore, these conformational changes after ATP hydrolysis may mostly happen in this part of the ion permeation pathway (see Discussion for detailed elaboration).

O_1 and O_2 states show different responses to MOPS⁻ block

To get a glimpse of possible structural differences between the O_1 and O_2 states, we used the anionic channel blocker MOPS⁻ to probe these two open states. We reasoned that the bulky part of MOPS⁻ is too large to pass the narrow region of the pore; thus, structural changes in the internal part of the pore during O_1 to O_2 transition may confer differential sensitivity of these two states to MOPS⁻ block as reported for WT channels (Ishihara and Welsh, 1997).

Fig. 8 A shows WT-CFTR current trace in the presence or absence of MOPS⁻. Indeed, two distinct current levels can be seen at 10-Hz filtering. This differential sensitivity to MOPS⁻ block is even more prominent with the mutant F311C/Cysless (Fig. 8 B). Although WT and F311C/Cysless constructs possess no additional charge in the internal vestibule, the mutant A299R with a net increase of one charge in

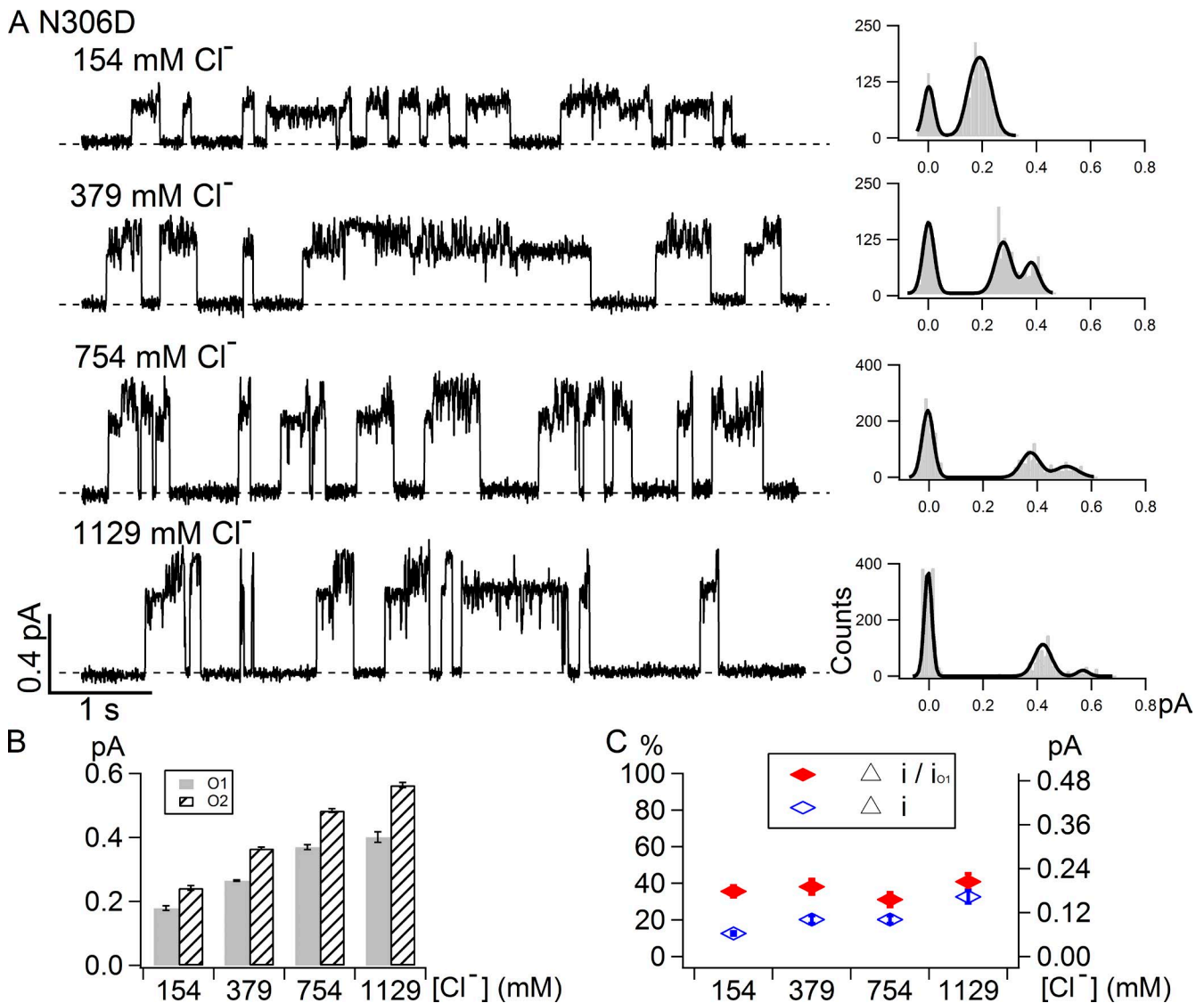


Figure 6. **Effects of cytoplasmic [Cl⁻] on the current amplitudes of the O₁ and O₂ states in N306D.** (A) Representative single-channel opening events of N306D under different intracellular chloride concentrations as marked with the corresponding all-points histograms on the right. The current amplitudes of both the O₁ state and O₂ state are increased with increasing chloride concentrations, but the difference between these two open states remains measurable even at the highest concentration tested (1,129 mM). (B) Summary of single-channel amplitudes of N306D at different cytoplasmic chloride concentrations. (C) Summary of normalized difference ($\Delta i/i_{O_1}$, left vertical axis) and absolute difference (Δi , right vertical axis) between the O₁ and O₂ states under different chloride concentrations.

the internal vestibule also exhibits two conductance levels in the presence of MOPS⁻, indicative of differential blockade of the O₁ and O₂ states by MOPS⁻ (raw trace not depicted, but see data in Fig. 9). Interestingly, even for M348R/R352Q where the single-channel amplitudes of O₁ and O₂ states are already clearly discernible in the absence of MOPS⁻, the O₁ state is also blocked more by MOPS⁻ compared with the O₂ state, resulting in an enlarged difference between the single-channel amplitudes of two open states (Fig. 8 C). However, this differential blocking effect of MOPS⁻ is diminished for mutants with an additional negative charge in the internal ves-

tibule. When we tested MOPS⁻ on two mutants, N306D and R303C/Cysless, where the internal vestibule loses one net charge, a uniform reduction of the current amplitude by MOPS⁻ was observed as if the O₁ and O₂ states of these two mutants show the same sensitivity to MOPS⁻ (Figs. 8 D and Fig. 9). Unlike WT and F311C/Cysless that have only one conductance without MOPS⁻ but show the O₁O₂ phenotype once blocked by MOPS⁻, R303C/Cysless with a net charge of negative one shows no O₁O₂ phenotype with or without MOPS⁻, which means both the O₁ state and O₂ state are equally blocked by MOPS⁻. The voltage-dependent nature of MOPS⁻-induced block is

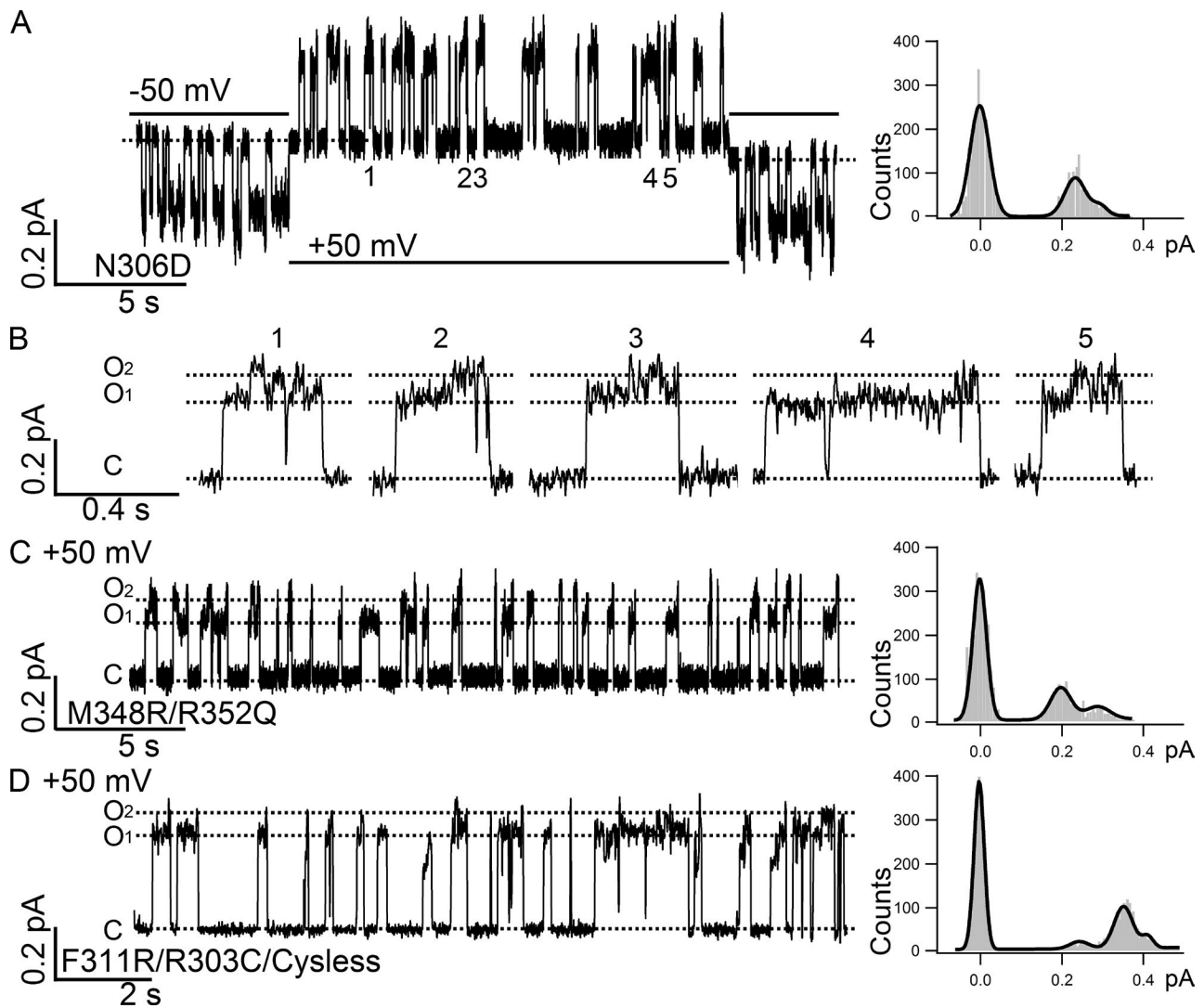


Figure 7. Effects of membrane potentials on the O_1O_2 phenotype. (A) A real-time single-channel recording of N306D upon voltage change from -50 mV (opening: downward deflections) to 50 mV (opening: upward deflections) showing the presence of clearly resolvable O_1 and O_2 states at ± 50 mV. The all-points histogram for the recording at 50 mV shows two discernible open states. (B) Opening bursts recorded at 50 mV indicated in A. Note the preferred gating topology of $C \rightarrow O_1 \rightarrow O_2 \rightarrow C$ is also seen at 50 mV. (C) A representative recording and its all-points histogram showing the existence of the O_1O_2 phenotype at 50 mV for M348R/R352Q. (D) The O_1O_2 phenotype at 50 mV and its all-points histogram for F311R/R303Q/Cysless. A third peak representing a smaller sub-conductance state is detected in the all-points histogram, which is also observed in all other CFTR mutations, including WT CFTR occasionally. However, the overall gating topology is still dominated by the O_1 and O_2 states. As described in the Materials and methods section, for a clearer data presentation, all single-channel traces recorded at negative membrane potentials were inverted except traces in this figure and Fig. 8 E, where conventional presentations were adopted.

demonstrated here with the example that no discernable changes of the single-channel amplitude were observed when 30 mM $MOPS^-$ was applied at 50 mV to the patch containing F311C/Cysless channels (Fig. 8 E). Fig. 9 summarizes this series of experiments demonstrating an intriguing effect of the net change of charge in the internal vestibule on the sensitivity of the O_1 and O_2 states to $MOPS^-$ block. In the Discussion, we attempt to propose a simple structural alteration during the O_1 to O_2 transition to explain most, if not all, of these seemingly perplexing observations.

DISCUSSION

O_1 and O_2 states are two conformations with distinct pore architectures

Decades of biophysical and biochemical studies have unveiled the intricate relationship between ATP acting on CFTR's two NBDs and gate opening/closing in its TMDs (Sohma and Hwang, 2015). In short, the opening of CFTR's gate is facilitated by ATP-induced dimerization of the two NBDs (Vergani et al., 2005). Because one ATP molecule can stay bound for tens of seconds in the catalysis-incompetent site (or site 1 com-

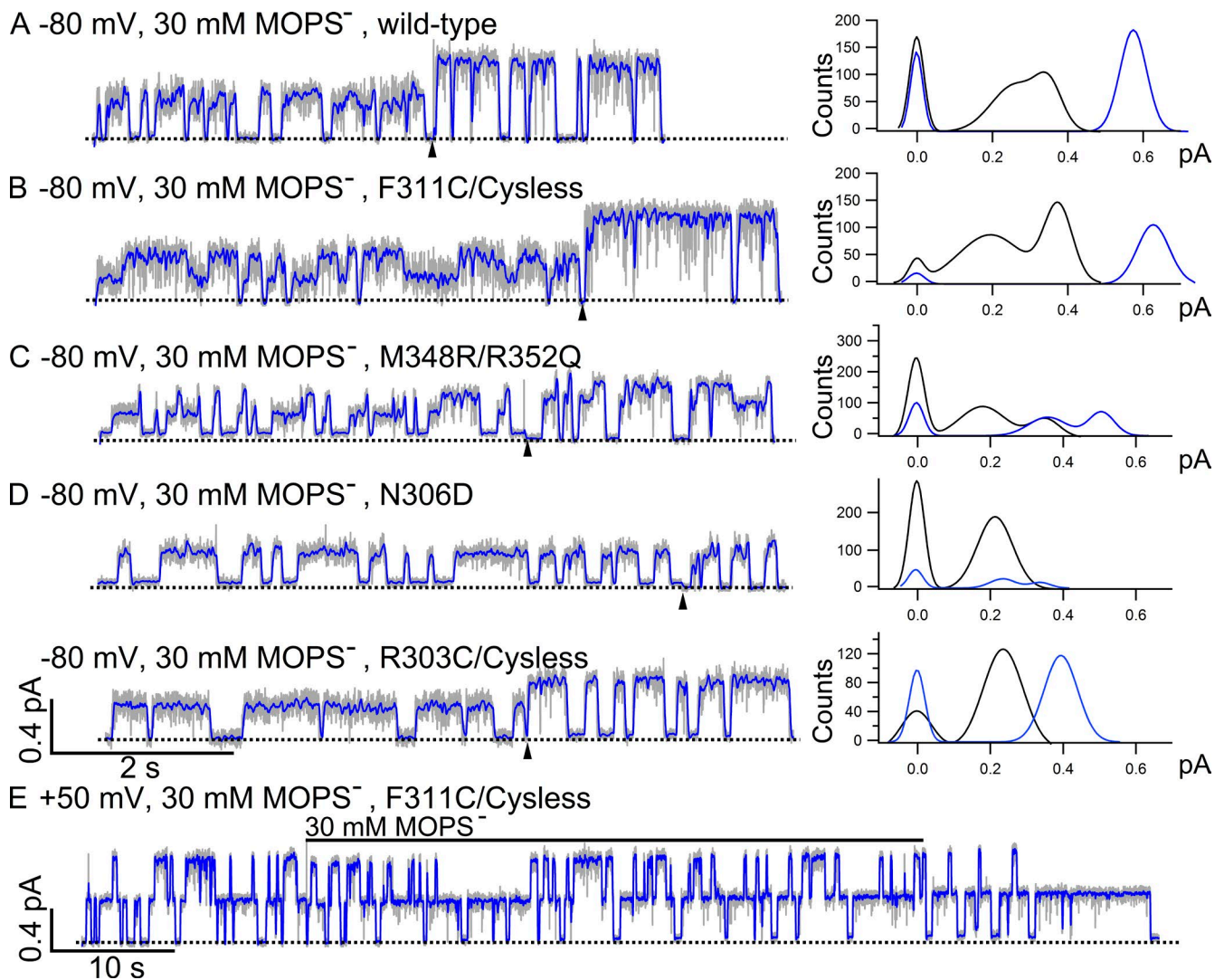


Figure 8. **O₁ and O₂ states exhibit differential sensitivity to channel-impermeant blocker MOPS⁻.** Current traces filtered at 100 Hz are shown as a gray background, whereas the same traces filtered at 10 Hz are colored in blue and super-positioned. For the traces in A–D, 30 mM MOPS⁻ was applied in the presence of 2 mM ATP in the early part of the recordings and then removed from the ATP-containing solution at the time point indicated by the arrowheads. The all-points histograms for the traces in the absence of MOPS⁻ are shown as blue curves, and the histograms for the traces in the presence of MOPS⁻ are shown as black curves. Dashed lines represent the baselines. (A) A representative trace of WT CFTR in the presence or absence of MOPS⁻. As reported previously (Ishihara and Welsh, 1997), two distinct open-channel conductance levels are clearly discerned once the data are filtered at 10 Hz. (B) Similar to WT CFTR that has only one resolvable open-channel conductance level in the presence of ATP, F311C/Cysless also shows two distinct open-channel conductance levels once blocked by MOPS⁻. (C) Amplification of the difference in single-channel amplitude between O₁ and O₂ states by MOPS⁻ in M348R/R352Q, which itself exhibits the O₁O₂ phenotype. The normalized difference ($\Delta i/i_{O_1}$) is $51 \pm 2\%$ without MOPS⁻ ($n = 9$) but $101 \pm 2\%$ with MOPS⁻ ($n = 4$). (D) Effects of net charge in the internal vestibule on the differential sensitivity of O₁ and O₂ states to MOPS⁻ block. Contrary to the results in A–C, N306D with one additional negative charge in the internal vestibule displays the O₁O₂ phenotype in the presence of ATP, but its O₁ and O₂ states show similar sensitivity to MOPS⁻ block. The O₂ states of N306D in the presence of MOPS⁻ could not be resolved by the all-points histogram because of its small single-channel amplitude and the brief open time of the O₂ state. Similar to N306D, R303C/Cysless also has one net charge deducted from the internal vestibule of CFTR's pore. For this mutant, however, only one open-channel level is seen in the absence or presence of MOPS⁻. (E) Compared with the result in B, the representative trace of F311C/Cysless recorded at 50 mV in the presence of 2 mM ATP shows negligible MOPS⁻ block.

posed of the head subdomain of NBD1 and the tail subdomain of NBD2), each observed closing after gate opening does not require dissociation of this tightly bound ATP at the dimer interface (Tsai et al., 2009, 2010; Csanády et al., 2010). Instead, closure of the chan-

nel is promoted by a partial separation of the NBD dimer after ATP hydrolysis at the catalysis-competent site (or site 2 formed by the head subdomain of NBD2 and the tail subdomain of NBD1; Vergani et al., 2003; Bompadre et al., 2005; but see Chaves and Gadsby,

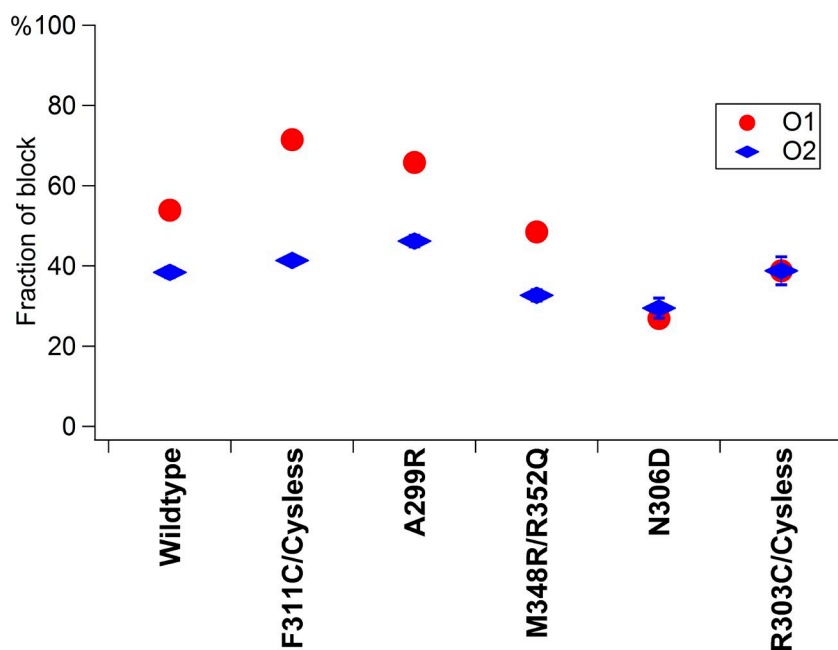


Figure 9. Summary of the fraction of block by MOPS^- at -80 mV for the data presented in Fig. 8. The O_1 state is more sensitive to MOPS^- than the O_2 state for mutants with the net charge in the internal vestibule unaltered or the positive one added. Using WT channels as a control, it appears that these mutations increase MOPS^- block of the O_1 state, not of the O_2 state. But for mutants with the net charge of minus one (N306D and R303C/Cysless), the O_1 and O_2 states are equally sensitive to MOPS^- . For some data points, the error bars are smaller than the symbol because of small SEM. $n = 3-4$.

2015). Although it remains debated whether the gating cycle is strictly coupled to the ATP hydrolysis cycle or not (Jih and Hwang, 2012), the molecular motion taking place in NBDs has to be transmitted to the gate in TMDs, as demonstrated previously (Sorum et al., 2015).

In this paper, we have identified several mutations/chemical modifications that result in channels exhibiting two distinct single-channel conductance levels, O_1 and O_2 , representing the pre- and post-hydrolytic open states of CFTR, respectively. Echoing our previous study (Jih and Hwang, 2012) showing that neutralizing the positively charged arginine at position 352 in TM6 creates channels (i.e., R352C or Q) with this characteristic behavior, here we found that introducing a negatively charged side chain to position 306 (i.e., N306D or E) in TM5 begets a similar O_1O_2 phenotype. As both N306 and R352 residues are located in the internal vestibule of CFTR's anion permeation pathway (Aubin and Linsdell, 2006; Bai et al., 2010; Zhang and Hwang, 2015; El Hiani et al., 2016; Zhang and Chen, 2016), our data suggest that a decrease of the number of net charge in these particular loci is important in establishing the conductance difference between the pre- and post-hydrolytic conformational states of CFTR. Furthermore, unlike R352C on TM6, the data that the mutation R303C (Fig. 8 D) itself does not display the O_1O_2 phenotype suggest that in addition to the number of net charges, the location of the charge is also critical in controlling the conductance level of each open state. The O_1O_2 phenotype observed when changing the location of the endogenously charged residues along TM6 (R352) or TM5 (R303) while maintaining the same net charge, together with the data in Fig. S2 showing that simply adding one positive charge at other pore-lining

residues (MTSET⁺-modified S307C/Cysless, F310C/Cysless, and F311C/Cysless) does not yield the O_1O_2 phenotype, further confirmed the importance of the charged position in imparting this characteristic gating/permeation behavior. Collectively, these results suggest that there is a conformational change of the open channel at the TMDs upon ATP hydrolysis at the NBDs. Thus, as proposed by Ishihara and Welsh (1997), the O_1 and the O_2 states represent two distinct conformations with different pore structures even for WT channels that do not show discernible differences in the single-channel conductance. Then, what could be the conformational change upon ATP hydrolysis?

The internal vestibule expands upon the O_1 to O_2 transition

Although the gating motions in NBDs upon ATP binding and hydrolysis have been elucidated to some extent, our understanding of the conformational changes in TMDs during gating is limited. Our recent studies using substituted cysteine accessibility methodology suggest some rearrangements of CFTR's TMs during each gating cycle (Bai et al., 2010, 2011; Gao et al., 2013). Notably, the current study shows that manipulating the number of the net charge as well as the position of the charged residues in the internal vestibule of the pore results in channels with clear differences in single-channel conductance between the O_1 and the O_2 states. In contrast, although numerous mutations have been made on residues comprising the external vestibule or the narrow region of CFTR's pore (Zhou et al., 2008; Cui et al., 2014), none confer the O_1O_2 phenotype. We thus argue for a major conformational change in the internal vestibule of the CFTR's pore upon ATP hydrolysis.

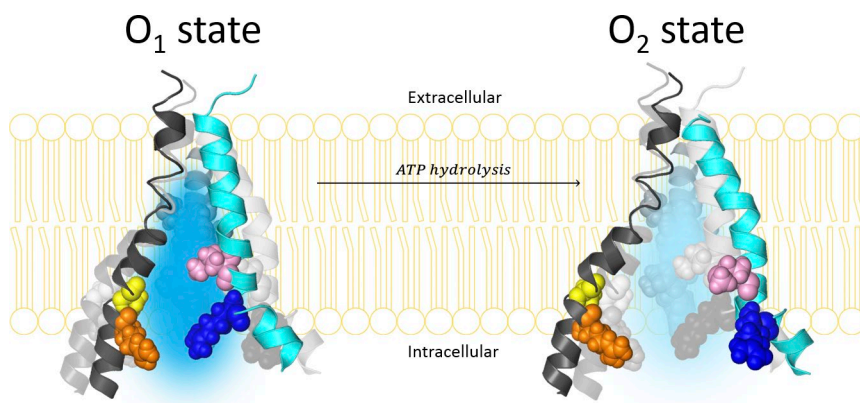


Figure 10. **Hypothetical expansion of the internal vestibule in CFTR's pore upon ATP hydrolysis-driven O_1 to O_2 transition.** TM6 (cyan), TM5 (black), and TM12 (dark gray) extracted from the homology model proposed by Dalton et al. (2012) are displayed in ribbon and rearranged purely for cosmetic purpose to illustrate a change of dimension in the internal vestibule of CFTR's pore in a cartoon style. In homology models or the cryo-EM structure of CFTR, the pore-lining TM5 and TM6 are not located at the exact opposite sides of the pore. Also, the depicted expansion of the internal vestibule by no means represents the real molecular motion during the O_1 (left) to O_2 (right) transition. Pore-lining res-

idues M348, R352, N306, and R303 are labeled in the spherical illustration with the same color code applied in Fig. 4. TM12 (dark gray) extracted from the same homology model is also displayed here along with the pore-lining residues (Bai et al., 2011) in a spherical illustration. From a macroscopic point of view, as the volume of the internal vestibule increases upon transition to the O_2 state, the local dielectric constant increases with the space filled with more water molecules. The electric field (both favorable and unfavorable) sensed by $MOPS^-$ is expected to dissipate more readily for the O_2 state. Differences in the local electric field between the O_1 and O_2 states subsequently result in different docking kinetic parameters for $MOPS^-$ block. To qualitatively depict the local electric field difference between the O_1 and O_2 states, we chose different densities of the positive electric field as an example (blue shadow of the internal vestibule): the darker the blue, the more positive the electric field. (Details are elaborated in the Discussion and supplemental materials).

Interestingly, compared with the open state, CFTR's closed channel conformation paradoxically assumes a wider internal entrance and perhaps a more expanded internal vestibule of the ion permeation pathway (Bai et al., 2011; Zhang and Hwang, 2015). Of note, the recently solved cryo-EM structure of zebrafish CFTR in a prephosphorylated closed conformation indeed shows a wide internal entrance between TM4 and TM6 (Zhang and Chen, 2016). This idea of a larger internal entrance is also consistent with the proposed molecular motions for ABC exporters, who share the evolutionary path with CFTR (Chen and Hwang, 2008; Gadsby, 2009; Rees et al., 2009). Specifically, because the NBD dimer of an ABC exporter is physically connected to its TMDs through the so-called coupling helices (Hollenstein et al., 2007), once ATP is hydrolyzed in NBDs, the separation of the NBD dimer may initiate the expansion of the helix bundle forming the internal gate—the structural equivalent to CFTR's internal entrance of the pore—of the transporter. Because the post-hydrolytic O_2 state chronologically lies between the prehydrolytic O_1 state and the closed state, we propose that the geometrical dimension of the internal vestibule is smaller in the O_1 state than in the O_2 state, if we accept the simplistic idea of a continuum of molecular motions of the internal vestibule upon transitions from open to closed states (Fig. 10).

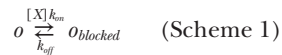
There are two possible consequences from the proposed smaller internal vestibule of the O_1 state. First, the residing charges are more densely packed, and a smaller space of the internal vestibule containing fewer water molecules to screen the electrostatic interactions between the positively charged vestibule and inhabiting

anions, in theory, could smooth down the dissipation of the electric field given out by the charged residues and subsequently magnify the electrostatic effect of charge manipulations in the internal vestibules that the negatively charged $MOPS^-$ will be attracted to. Second, a more restricted geometry of the pore implies a closer and stronger contact between the channel wall and the residing $MOPS^-$. In the next section, we will try to use these changes in physical properties during the O_1 to O_2 transition to explain the differential sensitivity to $MOPS^-$ block in mutants with the net change of charges of positive one or zero, such as WT, F311C/Cysless, A299R, and M348R/R352Q, but an equal sensitivity in mutants with a net change of charges of negative one, such as N306D and R303C. Because of limited space, here we only provide semiquantitative explanations for these seemingly perplexing results. Readers are referred to the supplemental materials for a more mathematical treatment of the same issue.

Amplified electrostatic effect in the O_1 state determines the differential sensitivity between the O_1 and O_2 states to $MOPS^-$ block

As a channel-impermeant blocker, $MOPS^-$ cannot penetrate deep through the narrow region of the pore because of its bulky size of $13 \text{ \AA} \times 7 \text{ \AA} \times 5.5 \text{ \AA}$ (Ishihara and Welsh, 1997). Although Scheme 1 depicts the simplest model for $MOPS^-$ -induced block, we prefer a three-state model Scheme 2 by introducing a docking process representing the diffusion of $MOPS^-$ from the bulk solution into the internal vestibule before the blocker traverses deeper into CFTR's pore. In this scheme, the O state is the only conduc-

tive state (see Figs. S3 and S4 for more extensive explanations). Of note, this three-state blocking theme has been successfully used to account for the blocking mechanism of CLC-0 chloride channels as well as the “ball-and-chain” inactivation mechanism of potassium channels (Zhou et al., 2001; Zhang and Chen, 2009; Zhang et al., 2009, 2010).



Mathematically, Scheme 2 yields the following formula for quantitatively describing the fraction of unblocking (F_{ub}) for the blocker MOPSS^- (indicated as $[X]$):

$$F_{ub} = \frac{1}{1 + \left[1 + \left(\frac{k_2}{k_{-2}}\right)\right] \cdot \left(\frac{k_1 \cdot [X]}{k_{-1}}\right)}.$$

Being a negatively charged blocker, MOPSS^- enters the internal vestibule of CFTR’s pore through a fast diffusion-like process with the docking (k_1) and undocking (k_{-1}) rates influenced by the electrostatic potential of the internal vestibule, which in this case is partly determined by the number of the net effective charge in the internal vestibule. Then the blocker leaves the docking site and moves deeper into the internal vestibule to form a direct contact with the wall of the pore perhaps with the charged group lodged in the narrow region or the selectivity filter to account for the high voltage dependence of the blockade. The rate of this blocking step (k_2) is not only expected to be slow and partially determined by the stability of MOPSS^- in the internal vestibule whose net charge is a deciding factor, but also determined by the geometry and chemistry of the pore. And the rate of the reverse process (k_{-2}), the presumed rate-limiting dissociation process of MOPSS^- from the O_{block} state, is mostly determined by the direct interactions between MOPSS^- and the wall in the deeper part—including perhaps the selectivity filter—of the pore.

For Scheme 2, which includes a docking step followed by a blocking step, the proposed larger geometrical dimension in the internal vestibule of the O_2 state results in a smaller blocking constant (k_2/k_{-2}) than that of the O_1 state because of a reduced contact between the blocker and the wall of the channel in the O_2 state (a larger k_{-2}). This blocking step is relatively insensitive to the net charge in the internal vestibule, which mainly affects the docking constant ($(k_1 \cdot [X])/k_{-1}$). For mutants with a net change of charges of plus one or zero in the internal vestibule that favors the docking step for MOPSS^- , the smaller dimension in the O_1 state provides a stronger electrostatic attractive force to yield a larger $(k_1 \cdot [X])/k_{-1}$. Thus, mathematically, the O_1 state is blocked more by MOPSS^- than the O_2 state, as both docking and blocking constants are higher for the O_1

state. In contrast, for those mutants with a net decrease of charges in the internal vestibule, e.g., N306D and R303C/Cysless, the electrostatic potential in the internal vestibule does not favor the docking step, and this “repulsive” force is stronger in the O_1 state because of the smaller size of the internal vestibule. Thus, in a way, the larger blocking constant (k_2/k_{-2}) for the O_1 state is effectively neutralized by the smaller docking constant ($(k_1 \cdot [X])/k_{-1}$) of the O_1 state for these mutants, accounting for an indistinguishable sensitivity to MOPSS^- block between the O_1 and O_2 states. Even if there might be a small difference in the final F_{ub} between the O_1 and O_2 state, this difference would be too small to be resolved given the reduced single-channel amplitudes for mutants with one additional negative charge (see Supplemental Materials for detailed elaborations and a set of kinetic simulation parameters that actually fits our experimental observation).

Normal chloride permeation requires cross talk among multiple residues in the internal vestibule

What has been elaborated in the last section offers a simplified—admittedly over-simplified—picture of the expansion movement in CFTR’s pore upon ATP hydrolysis to explain the effects of MOPSS^- . Now, we attempt to use the molecular insights out of the atomic structure of zebrafish CFTR (Zhang and Chen, 2016) to explain why WT channels show no obvious conductance difference between the O_1 and O_2 states when chloride ion is the charge carrier, whereas those mutations such as N306D, M348R/R352Q, and F310R/R303C/Cysless do.

Unlike measuring equilibrium block by the bulky impermeant MOPSS^- , the single-channel amplitude reflects a nonequilibrium condition when a net anion flux occurs through the pore. From the free-energy point of view, the whole ion translocation process, from entering the cytoplasmic mouth, passing along the internal vestibule, and finally penetrating through the selectivity filter, has to be energetically favored and well balanced. This process will involve the cross talk among multiple residues from different TMs by a short-range cooperation among local residues, solvent, water molecules, and other chloride ions or a long-range coupling mechanism, through which the perturbation at a large distance also modifies the local free energy surface (Läuger, 1979; Bernèche and Roux, 2001).

We do not know the exact details determining the free energy profile for chloride permeation in the O_1 and O_2 states. However, the aforementioned idea based on changes in the electrostatics of the internal vestibule may be also responsible for the different single-channel amplitudes seen with the O_1 and O_2 states because this particular phenotype is conferred by a change of the charge location in TM5 or TM6. Of note, the cryo-EM structure of zebrafish CFTR suggests several candidate

local charge networks in CFTR's internal vestibule. The one that draws our attention is the network between R352 (TM6) and D993 (TM9). Specifically, this network between R352 and D993 lines right at the shoulder of the internal vestibule where the internal vestibule starts to taper down to a narrower region according to the cryo-EM structure (Fig. 4 A; Zhang and Chen, 2016). Although the cryo-EM study caught the CFTR in a pre-phosphorylated closed state, this salt bridge between R352 and D993 is likely also present in the open state (Cui et al., 2008; Jordan et al., 2008). This critical location of R352/D993 charge network in the ion permeation path may explain why the electronegative potential caused by mutation-induced subtraction of a positive charge (e.g., R352Q) decreases the single-channel conductance. Furthermore, the same electronegative potential will exert a larger effect on chloride permeation in the O₁ state with a smaller dimension, as proposed in the current study, than the O₂ state (i.e., the O₁O₂ phenotype). The same concept of precise charge balance between R352 and D993 may also explain why M348R/R352Q still exhibits the O₁O₂ phenotype albeit a high single-channel conductance compared with that of R352Q; after all, M348 is farther from D993 than R352 (Fig. 4 B). This idea of balanced local charge network also leads us to reason that the characteristic O₁O₂ phenotype seen in N306D and N306E mutants is caused by a disruption of the same network, as N306 is located in the vicinity of R352 and D993 with the following distances in between: 12.7 Å (R352 and N306), 12.2 Å (N306 and D993), and 14.8 Å (D993 and R352; Fig. 4 C; Zhang and Chen, 2016). This hypothesis predicts a superposition of electric fields produced by the charges at D306 and D993. Consistent with this idea, neutralizing D993 under the N306D background (N306D/D993N; Fig. S5) increases the single-channel amplitudes of both O₁ and O₂ states and decreases the difference in single-channel amplitude between these two states.

How moving the endogenous positive charge at position 303 along TM5 confers the O₁O₂ phenotype is a more difficult question to answer because neutralization of R303, although it does decrease the single-channel conductance, fails to yield different open states. Interestingly, however, the cryo-EM structure of CFTR does reveal several charged amino acids near R303: R248 (12.5 Å), R251 (15.4 Å), D985 (11.7 Å), and D984 (14.5 Å; Zhang and Chen, 2016). In addition, contrary to the positions of R352 and D993 where the internal vestibule starts to taper down to the narrow region of the pore, R303 is positioned more cytoplasmically in the more spacious region of the internal vestibule (Fig. 4 B). Perhaps a wider space lessens the electrostatic effect of dimensional changes during the O₁ to O₂ transition. Furthermore, as different regions of the internal vestibule show different

charge distributions as well as physical contours (Fig. 4 B; Zhang and Chen, 2016), it seems unsurprising that perturbations of local electrostatics may exhibit different O₁O₂ phenotypes (Figs. 1, 2, 3, 5, S5 and S6).

In short, we speculate that a detailed balance of the charge network between R352 and D993 (and likely also other charge networks), which the permeating chloride will encounter at a fairly narrow region of the pore, accounts for a lack of the O₁O₂ phenotype in WT channels. On the contrary, once this charge network is perturbed by mutations and/or chemical modifications, the unbalanced electrostatic potential profile in this region will exert effects on the incoming/exiting chloride ions. Just like the mechanism we have elaborated for MOPS⁻ block, the magnitude of this electrostatic effect will depend on the physical dimension of the internal vestibule. Once the atomic structure of CFTR's open state is solved, one can start to explore the biophysical function of charged networks in chloride permeation through CFTR.

The coupling mechanism of CFTR gating and the conformational changes during gating transitions are among the most interesting topics in the CFTR field. Apparently many more experiments are needed to bequeath us a deeper understanding of this subject. Although we may still be far from getting a close glimpse of the crystal structure of CFTR, the current study provides insights into the role of charged residues and their positions in determining anion permeation in the pore of CFTR. Furthermore, a larger toolbox for the mechanistic studies of CFTR gating by ATP hydrolysis is now becoming available.

ACKNOWLEDGMENTS

We thank Cindy Chu and Shenghui Hu for their technical assistance. We are grateful to Dr. Jue Chen for kindly providing us the coordinate of the cryo-EM structure of zebrafish CFTR.

This work is supported by the National Institutes of Health (grant NIH01DK55835) and the Cystic Fibrosis Foundation (grant Hwang11P0) to T.-C. Hwang. During the course of this study, 5% of T.-C. Hwang's salary was supported by Vertex Pharmaceutical Inc.

The authors declare no additional competing financial interests.

Author contributions: Conception and design of experiments, J. Zhang and T.-C. Hwang; collection and analysis of data, J. Zhang; interpretation of data, J. Zhang and T.-C. Hwang; drafting the article or revising it critically for important intellectual content, J. Zhang and T.-C. Hwang. It is confirmed that both authors approved the final version of the manuscript and that all persons designated as authors qualify for authorship, and all those who qualify for authorship are listed. All experiments were performed in the Dalton Cardiovascular Research Center, University of Missouri – Columbia.

Merritt C. Maduke served as editor.

Submitted: 8 July 2016

Revised: 17 November 2016

Accepted: 20 January 2017

REFERENCES

- Aubin, C.N., and P. Linsdell. 2006. Positive charges at the intracellular mouth of the pore regulate anion conduction in the CFTR chloride channel. *J. Gen. Physiol.* 128:535–545. <http://dx.doi.org/10.1085/jgp.200609516>
- Bai, Y., M. Li, and T.C. Hwang. 2010. Dual roles of the sixth transmembrane segment of the CFTR chloride channel in gating and permeation. *J. Gen. Physiol.* 136:293–309. <http://dx.doi.org/10.1085/jgp.201010480>
- Bai, Y., M. Li, and T.C. Hwang. 2011. Structural basis for the channel function of a degraded ABC transporter, CFTR (ABCC7). *J. Gen. Physiol.* 138:495–507. <http://dx.doi.org/10.1085/jgp.201110705>
- Beard, C.E., C.H. Li, N. Kartner, R.J. Bridges, T.J. Jensen, M. Ramjeesingh, and J.R. Riordan. 1992. Purification and functional reconstitution of the cystic fibrosis transmembrane conductance regulator (CFTR). *Cell.* 68:809–818. [http://dx.doi.org/10.1016/0092-8674\(92\)90155-6](http://dx.doi.org/10.1016/0092-8674(92)90155-6)
- Bernèche, S., and B. Roux. 2001. Energetics of ion conduction through the K⁺ channel. *Nature.* 414:73–77. <http://dx.doi.org/10.1038/35102067>
- Bompadre, S.G., J.H. Cho, X. Wang, X. Zou, Y. Sohma, M. Li, and T.C. Hwang. 2005. CFTR gating II: Effects of nucleotide binding on the stability of open states. *J. Gen. Physiol.* 125:377–394. <http://dx.doi.org/10.1085/jgp.200409228>
- Bozoky, Z., M. Krzeminski, R. Muhandiram, J.R. Birtley, A. Al-Zahrani, P.J. Thomas, R.A. Frizzell, R.C. Ford, and J.D. Forman-Kay. 2013. Regulatory R region of the CFTR chloride channel is a dynamic integrator of phospho-dependent intra- and intermolecular interactions. *Proc. Natl. Acad. Sci. USA.* 110:E4427–E4436. <http://dx.doi.org/10.1073/pnas.1315104110>
- Chaves, L.A., and D.C. Gadsby. 2015. Cysteine accessibility probes timing and extent of NBD separation along the dimer interface in gating CFTR channels. *J. Gen. Physiol.* 145:261–283. <http://dx.doi.org/10.1085/jgp.201411347>
- Chen, T.Y., and T.C. Hwang. 2008. CLC-0 and CFTR: chloride channels evolved from transporters. *Physiol. Rev.* 88:351–387. <http://dx.doi.org/10.1152/physrev.00058.2006>
- Csanády, L., P. Vergani, and D.C. Gadsby. 2010. Strict coupling between CFTR's catalytic cycle and gating of its Cl⁻ ion pore revealed by distributions of open channel burst durations. *Proc. Natl. Acad. Sci. USA.* 107:1241–1246. <http://dx.doi.org/10.1073/pnas.0911061107>
- Cui, G., Z.R. Zhang, A.R. O'Brien, B. Song, and N.A. McCarty. 2008. Mutations at arginine 352 alter the pore architecture of CFTR. *J. Membr. Biol.* 222:91–106. <http://dx.doi.org/10.1007/s00232-008-9105-9>
- Cui, G., K.S. Rahman, D.T. Infield, C. Kuang, C.Z. Prince, and N.A. McCarty. 2014. Three charged amino acids in extracellular loop 1 are involved in maintaining the outer pore architecture of CFTR. *J. Gen. Physiol.* 144:159–179. <http://dx.doi.org/10.1085/jgp.201311122>
- Dalton, J., O. Kalid, M. Schushan, N. Ben-Tal, and J. Villà-Freixa. 2012. New model of cystic fibrosis transmembrane conductance regulator proposes active channel-like conformation. *J. Chem. Inf. Model.* 52:1842–1853. <http://dx.doi.org/10.1021/ci2005884>
- Davidson, A.L., and P.C. Maloney. 2007. ABC transporters: how small machines do a big job. *Trends Microbiol.* 15:448–455. <http://dx.doi.org/10.1016/j.tim.2007.09.005>
- El Hiani, Y., and P. Linsdell. 2012. Tuning of CFTR chloride channel function by location of positive charges within the pore. *Biophys. J.* 103:1719–1726. <http://dx.doi.org/10.1016/j.bpj.2012.09.020>
- El Hiani, Y., A. Negoda, and P. Linsdell. 2016. Cytoplasmic pathway followed by chloride ions to enter the CFTR channel pore. *Cell. Mol. Life Sci.* 73:1917–1925. <http://dx.doi.org/10.1007/s00018-015-2113-x>
- Gadsby, D.C. 2009. Ion channels versus ion pumps: the principal difference, in principle. *Nat. Rev. Mol. Cell Biol.* 10:344–352. <http://dx.doi.org/10.1038/nrm2668>
- Gadsby, D.C., P. Vergani, and L. Csanády. 2006. The ABC protein turned chloride channel whose failure causes cystic fibrosis. *Nature.* 440:477–483. <http://dx.doi.org/10.1038/nature04712>
- Gao, X., Y. Bai, and T.C. Hwang. 2013. Cysteine scanning of CFTR's first transmembrane segment reveals its plausible roles in gating and permeation. *Biophys. J.* 104:786–797. <http://dx.doi.org/10.1016/j.bpj.2012.12.048>
- Gunderson, K.L., and R.R. Kopito. 1995. Conformational states of CFTR associated with channel gating: the role ATP binding and hydrolysis. *Cell.* 82:231–239. [http://dx.doi.org/10.1016/0092-8674\(95\)90310-0](http://dx.doi.org/10.1016/0092-8674(95)90310-0)
- Higgins, C.F., and K.J. Linton. 2004. The ATP switch model for ABC transporters. *Nat. Struct. Mol. Biol.* 11:918–926. <http://dx.doi.org/10.1038/nsmb836>
- Hollenstein, K., R.J.P. Dawson, and K.P. Locher. 2007. Structure and mechanism of ABC transporter proteins. *Curr. Opin. Struct. Biol.* 17:412–418. <http://dx.doi.org/10.1016/j.sbi.2007.07.003>
- Hwang, T.C., and K.L. Kirk. 2013. The CFTR ion channel: gating, regulation, and anion permeation. *Cold Spring Harb. Perspect. Med.* 3:a009498. <http://dx.doi.org/10.1101/cshperspect.a009498>
- Hwang, T.C., and D.N. Sheppard. 2009. Gating of the CFTR Cl⁻ channel by ATP-driven nucleotide-binding domain dimerisation. *J. Physiol.* 587:2151–2161. <http://dx.doi.org/10.1113/jphysiol.2009.171595>
- Ishihara, H., and M.J. Welsh. 1997. Block by MOPS reveals a conformation change in the CFTR pore produced by ATP hydrolysis. *Am. J. Physiol.* 273:C1278–C1289.
- Jih, K.Y., and T.C. Hwang. 2012. Nonequilibrium gating of CFTR on an equilibrium theme. *Physiology (Bethesda).* 27:351–361. <http://dx.doi.org/10.1152/physiol.00026.2012>
- Jih, K.Y., Y. Sohma, and T.C. Hwang. 2012. Nonintegral stoichiometry in CFTR gating revealed by a pore-lining mutation. *J. Gen. Physiol.* 140:347–359. <http://dx.doi.org/10.1085/jgp.201210834>
- Jordan, I.K., K.C. Kota, G. Cui, C.H. Thompson, and N.A. McCarty. 2008. Evolutionary and functional divergence between the cystic fibrosis transmembrane conductance regulator and related ATP-binding cassette transporters. *Proc. Natl. Acad. Sci. USA.* 105:18865–18870. <http://dx.doi.org/10.1073/pnas.0806306105>
- Kathawala, R.J., P. Gupta, C.R. Ashby Jr., and Z.S. Chen. 2015. The modulation of ABC transporter-mediated multidrug resistance in cancer: a review of the past decade. *Drug Resist. Updat.* 18:1–17. <http://dx.doi.org/10.1016/j.drug.2014.11.002>
- Läuger, P. 1979. A channel mechanism for electrogenic ion pumps. *Biochim. Biophys. Acta.* 552:143–161. [http://dx.doi.org/10.1016/0005-2736\(79\)90253-0](http://dx.doi.org/10.1016/0005-2736(79)90253-0)
- Li, Y., W.-P. Yu, C.-W. Lin, and T.-Y. Chen. 2005. Oxidation and reduction control of the inactivation gating of Torpedo ClC-0 chloride channels. *Biophys. J.* 88:3936–3945. <http://dx.doi.org/10.1529/biophysj.104.055012>
- Liu, X., C. Alexander, J. Serrano, E. Borg, and D.C. Dawson. 2006. Variable reactivity of an engineered cysteine at position 338 in cystic fibrosis transmembrane conductance regulator reflects different chemical states of the thiol. *J. Biol. Chem.* 281:8275–8285. <http://dx.doi.org/10.1074/jbc.M512458200>
- Locher, K.P. 2009. Structure and mechanism of ATP-binding cassette transporters. *Philos. Trans. R. Soc. Lond. B Biol. Sci.* 364:239–245. <http://dx.doi.org/10.1098/rstb.2008.0125>
- Mornon, J.P., B. Hoffmann, S. Jonic, P. Lehn, and I. Callebaut. 2015. Full-open and closed CFTR channels, with lateral tunnels from the cytoplasm and an alternative position of the F508 region, as

- revealed by molecular dynamics. *Cell. Mol. Life Sci.* 72:1377–1403. <http://dx.doi.org/10.1007/s00018-014-1749-2>
- Oldham, M.L., A.L. Davidson, and J. Chen. 2008. Structural insights into ABC transporter mechanism. *Curr. Opin. Struct. Biol.* 18:726–733. <http://dx.doi.org/10.1016/j.sbi.2008.09.007>
- Ostedgaard, L.S., O. Baldursson, D.W. Vermeer, M.J. Welsh, and A.D. Robertson. 2000. A functional R domain from cystic fibrosis transmembrane conductance regulator is predominantly unstructured in solution. *Proc. Natl. Acad. Sci. USA.* 97:5657–5662. <http://dx.doi.org/10.1073/pnas.100588797>
- Ostedgaard, L.S., O. Baldursson, and M.J. Welsh. 2001. Regulation of the cystic fibrosis transmembrane conductance regulator Cl⁻ channel by its R domain. *J. Biol. Chem.* 276:7689–7692. <http://dx.doi.org/10.1074/jbc.R100001200>
- Rees, D.C., E. Johnson, and O. Lewinson. 2009. ABC transporters: the power to change. *Nat. Rev. Mol. Cell Biol.* 10:218–227. <http://dx.doi.org/10.1038/nrm2646>
- Riordan, J.R., J.M. Rommens, B. Kerem, N. Alon, R. Rozmahel, Z. Grzelczak, J. Zielenski, S. Lok, N. Plavsic, J.L. Chou, et al. 1989. Identification of the cystic fibrosis gene: cloning and characterization of complementary DNA. *Science.* 245:1066–1073. <http://dx.doi.org/10.1126/science.2475911>
- Sohma, Y., and T.C. Hwang. 2015. Cystic fibrosis and the CFTR anion channel. In *Handbook of Ion Channels*. Vol. 627. Zheng and M.C. Trudeau, editors. CRC Press, Boca Taton, FL. 627–648. <http://dx.doi.org/10.1201/b18027-48>
- Sorum, B., D. Czégé, and L. Csanády. 2015. Timing of CFTR pore opening and structure of its transition state. *Cell.* 163:724–733. <http://dx.doi.org/10.1016/j.cell.2015.09.052>
- Tsai, M.F., H. Shimizu, Y. Sohma, M. Li, and T.C. Hwang. 2009. State-dependent modulation of CFTR gating by pyrophosphate. *J. Gen. Physiol.* 133:405–419. <http://dx.doi.org/10.1085/jgp.200810186>
- Tsai, M.F., M. Li, and T.C. Hwang. 2010. Stable ATP binding mediated by a partial NBD dimer of the CFTR chloride channel. *J. Gen. Physiol.* 135:399–414. <http://dx.doi.org/10.1085/jgp.201010399>
- Vergani, P., A.C. Nairn, and D.C. Gadsby. 2003. On the mechanism of MgATP-dependent gating of CFTR Cl⁻ channels. *J. Gen. Physiol.* 121:17–36. <http://dx.doi.org/10.1085/jgp.20028673>
- Vergani, P., S.W. Lockless, A.C. Nairn, and D.C. Gadsby. 2005. CFTR channel opening by ATP-driven tight dimerization of its nucleotide-binding domains. *Nature.* 433:876–880. <http://dx.doi.org/10.1038/nature03313>
- Zhang, J., and T.C. Hwang. 2015. The fifth transmembrane segment of cystic fibrosis transmembrane conductance regulator contributes to its anion permeation pathway. *Biochemistry.* 54:3839–3850. <http://dx.doi.org/10.1021/acs.biochem.5b00427>
- Zhang, X.D., and T.Y. Chen. 2009. Amphiphilic blockers punch through a mutant CLC-0 pore. *J. Gen. Physiol.* 133:59–68. <http://dx.doi.org/10.1085/jgp.200810005>
- Zhang, Z., and J. Chen. 2016. Atomic structure of the cystic fibrosis transmembrane conductance regulator. *Cell.* 167:1586–1597.e9. <http://dx.doi.org/10.1016/j.cell.2016.11.014>
- Zhang, X.D., P.Y. Tseng, W.P. Yu, and T.Y. Chen. 2009. Blocking pore-open mutants of CLC-0 by amphiphilic blockers. *J. Gen. Physiol.* 133:43–58. <http://dx.doi.org/10.1085/jgp.200810004>
- Zhang, X.D., W.P. Yu, and T.Y. Chen. 2010. Accessibility of the CLC-0 pore to charged methanethiosulfonate reagents. *Biophys. J.* 98:377–385. <http://dx.doi.org/10.1016/j.bpj.2009.09.066>
- Zhou, J.J., and P. Linsdell. 2007. Molecular mechanism of arachidonic acid inhibition of the CFTR chloride channel. *Eur. J. Pharmacol.* 563:88–91. <http://dx.doi.org/10.1016/j.ejphar.2007.02.048>
- Zhou, J.J., M. Fatehi, and P. Linsdell. 2008. Identification of positive charges situated at the outer mouth of the CFTR chloride channel pore. *Pflugers Arch.* 457:351–360. <http://dx.doi.org/10.1007/s00424-008-0521-6>
- Zhou, J.J., M.S. Li, J. Qi, and P. Linsdell. 2010. Regulation of conductance by the number of fixed positive charges in the intracellular vestibule of the CFTR chloride channel pore. *J. Gen. Physiol.* 135:229–245. <http://dx.doi.org/10.1085/jgp.200910327>
- Zhou, M., J.H. Morais-Cabral, S. Mann, and R. MacKinnon. 2001. Potassium channel receptor site for the inactivation gate and quaternary amine inhibitors. *Nature.* 411:657–661. <http://dx.doi.org/10.1038/35079500>